Temporal variability in the Holocene marine radiocarbon reservoir effect for the Tropical and South Pacific

Quan Hua[a,*], Sean Ulm[b], Kefu Yu[c,d], Tara R. Clark[e,f], Luke D. Nothdurft[g], Nicole D. Leonard[f], John M. Pandolfi[h], Geraldine E. Jacobsen[a], Jian-xin Zhao[f]

[a]Australian Nuclear Science and Technology Organisation, Locked Bag 2001, Kirrawee DC, NSW 2232, Australia

[b]ARC Centre of Excellence for Australian Biodiversity and Heritage, College of Arts, Society and Education, James Cook University, PO Box 6811, Cairns, QLD 4870, Australia

[c]Guangxi Laboratory on the Study of Coral Reefs in the South China Sea and Coral Reef Research Centre of China, Guangxi University, Nanning, China

[d]Southern Marine Science and Engineering Guangdong Laboratory (Zhuhai), China

[e]School of Earth, Atmospheric and Life Sciences, University of Wollongong, Northfields Avenue, Wollongong, NSW 2522, Australia

[f]School of Earth and Environmental Sciences, The University of Queensland, Brisbane, QLD 4072, Australia

[g]School of Earth and Atmospheric Sciences, Queensland University of Technology, GPO Box 2434, Brisbane, QLD 4001, Australia

[h]ARC Centre of Excellence for Coral Reef Studies, School of Biological Sciences, The University of Queensland, Brisbane, QLD 4072, Australia

*Corresponding author. Email: qhx@ansto.gov.au

Highlights

- New ΔR for Western Pacific for ~0-8 ka based on ^{14}C analysis of ^{230}Th-dated corals
- ΔR variability of ~200-490 yr for Western Pacific during the last ~8 ka
- ΔR variability of ~300-1000 yr for coastal Eastern Pacific during the last ~12 ka
- ΔR variations are mainly due to large scale climate and ocean circulation changes
- Urgent need for local/regional marine calibration curves for improved ^{14}C dating

Abstract

Understanding the marine radiocarbon reservoir effect (i.e., marine radiocarbon reservoir age (R) and/or correction (ΔR)) is important for the construction of robust radiocarbon chronologies for marine archives for various research areas including archaeology, palaeoecology, paleoceanography, Quaternary research and climate change studies. In this study, we examined temporal ΔR variability for the South China Sea (SCS) and the Great Barrier Reef (GBR) during the past ~8.1 ka based on ^{14}C analysis of ^{230}Th-dated corals. Results show large ΔR variations of ~410 yr and ~490 yr for the SCS and the northern GBR for ~5.5-8.1 ka and ~5.5-7 ka, respectively, and a smaller ΔR variability of ~200 yr for the SCS for ~2-3.5 ka. Our data together with those previously published for the Tropical and South Pacific indicate that variability in ocean upwelling bringing old subsurface waters to the surface and/or changes in the sources (or ^{14}C level) of the upwelled waters are responsible for seeing large ΔR variations in coastal areas along the eastern Pacific and the Tropical East Pacific (TEP) of several hundred to a thousand years mostly during the Early to Middle Holocene. ΔR variations in the central and western Pacific of several and a couple of hundred years during the Middle and Late Holocene, respectively, might be due to variability in Pacific-wide ocean circulation associated with climatic changes controlling the spread of upwelled waters from the TEP to the west. This mechanism together with local/regional effects such as changes in ocean upwelling in the SCS resulting from East Asian monsoon variability and changes in upwelling and/or horizontal advection in the northern GBR associated with variability in the El Niño Southern Oscillation might be responsible for the observed ΔR variations in these areas. The results of our study also indicate the need for regional marine radiocarbon calibration curves for improved radiocarbon dating of marines samples as the observed Holocene ΔR values for the Tropical and South Pacific are not fully reproduced by a recent modelling work using a 3D ocean model, which takes into account climate change effects. Ocean circulation changes were considered in the model for the period of 11.5-50 cal. kyr BP but possibly not well represented for the Holocene, which might explain the differences between the observed and modelled ΔR values.

Keywords

marine radiocarbon reservoir effect, ΔR, ocean circulation, climate change, Holocene, corals, Pacific Ocean, U-Th dating

1. Introduction

Radiocarbon (^{14}C) chronologies constructed for marine samples are not straightforward as for terrestrial samples, which once lived in equilibrium with atmospheric ^{14}C. Surface ocean samples (e.g., molluscs, corals, coralline algae and planktonic foraminifera) are subject to the marine radiocarbon reservoir effect (or simply the marine reservoir effect, MRE) due to the long residence time of carbon in the oceans, resulting in older ^{14}C ages for these marine samples compared to terrestrial samples of the same age. The MRE, expressed as either marine radiocarbon reservoir age (R) or local/regional marine radiocarbon reservoir correction (ΔR), must be estimated for ^{14}C dating and calibration of marine samples. There are several methods for reliable determination of R and ΔR values including the use of pre-bomb known-age historical marine specimens, dated corals by either band counting or U-Th, paired terrestrial/marine samples, and planktonic foraminifera in deep-sea cores. Details of these methods and their associated criteria are summarised in Table 1.

Traditionally, R and ΔR are assumed to be constant through time and their modern values are employed for age calibration of surface ocean samples (e.g., Stuiver et al., 1986; Alves et al., 2018). However, there is growing evidence that these values are not constant but vary with time. Temporal variations in these values have been documented for a number of oceans and seas (Sikes et al., 2000; Siani et al., 2001; van Beek et al., 2002; Bondevik et al., 2006; Hua et al., 2009; Skinner et al., 2015; Sarnthein et al., 2015; Lindauer et al., 2017; Toth et al., 2017). For the Pacific Ocean, large temporal R and/or ΔR variations of several hundred to almost a thousand of years were reported for a number of Holocene sites, including the Gulf of Panama (Toth et al., 2015), southern Peru – northern Chile (Ortlieb et al., 2011; Latorre et al., 2017), central Chile (Carré et al., 2016), the South China Sea (SCS, Yu et al., 2010; Hirabayashi et al., 2019), Papua New Guinea (PNG, McGregor et al., 2008; Burr et al., 2015), Solomon Islands (Burr et al., 2015), Heron Reef in the southern Great Barrier Reef (GBR) and Moreton Bay in southeastern Queensland, Australia (Hua et al., 2015), and off the Tasman coast in southeastern Australia (Komugabe-Dixson et al., 2016).

Here we report new values for the MRE for the SCS, and the northern and southern GBR during the past ca. 8.1 cal. kyr before present (BP, with 0 BP being AD 1950) derived from ^{14}C analysis of ^{230}Th-dated corals. Based on these new data and those previously published, we discuss temporal variations in this effect not only for our study sites but also for the wider Pacific, including the Tropical and South Pacific, and their implications for ocean circulation variability associated with climatic changes during the Holocene. We then compare these wider Pacific MRE data to the MRE evolution modelled by Butzin et al. (2017) using a 3D ocean model that takes into account effects of climate change, and discuss how our study results in improved ^{14}C dating of Holocene marine samples for this region.

Table 1. Methods and associated criteria for reliable determination of the marine radiocarbon reservoir effect.

Methods	Criteria	References
Pre-bomb (pre-AD, 1950) historical marine specimens	Live collected	Southon et al. (2002)
	Known location and date of collection	Petchey (2009)
	Suspension or filter feeders (shellfish)	O'Connor et al. (2010) Hua (2015)
Modern corals with clear growth bands	Annual density bands detected with X-radiography	Druffel (1997)
	Annual fluorescent bands visible under UV light	Dang et al. (2004)
	Seasonal variability in coral $\delta^{13}C$ and/or $\delta^{18}O$	Hua et al. (2004)
U-Th dated corals	XRD (<1% calcite) and/or SEM screening on carbonate skeleton	Reimer et al. (2009)
	Initial $\delta^{234}U$ of modern sea water of 147 ± 5‰	Yu et al. (2010)
	High initial $^{230}Th/^{232}Th$ indicating low non-radiogenic ^{230}Th	Hua et al. (2015)
Paired terrestrial/marine samples	Short-lived macrofossils	Ulm (2002)
	If charcoal is used, species identification is required to avoid the "old wood" problem	Bondevik et al. (2006)
	Suspension or filter feeders (shellfish)	Ascough et al. (2009)
	Whole individual shells to minimise the use of re-worked material	Ortlieb et al. (2011)
	Multiple paired sample approach	Latorre et al. (2017)
Planktonic foraminifera in deep-sea cores	Mono species are preferable	Sarnthein et al. (2015)

2. Material and methods

2.1. Study sites and modern oceanographic settings

The SCS, located in Southeast Asia, is a marginal sea connecting to the Pacific Ocean (Fig. 1). The SCS is strongly influenced by Asian monsoons and is very sensitive to other climate forcings including the El Niño Southern Oscillation (ENSO) and Pacific decadal variability (Yu et al., 2004; Wang et al., 2005; Yancheva et al., 2007; Hu et al., 2015). Surface waters reaching the SCS originate from the North Equatorial Current (NEC). Upon arriving at the Philippine coast, the westward-flowing NEC bifurcates at ~15.5°N into the southward-flowing Mindanao Current and the northward-flowing Kuroshio Current, a portion of which flows into the SCS through the deep and wide Luzon Strait (Fig. 1). Our study sites are Yongxing Island (16°50′N, 112°20′E) in the Xisha (or Paracel) Islands in the northwestern SCS, and Yongshu Reef (9°32′- 9°42′N, 112°52′-113°04′E) in the Nansha (or Spratly) Islands in the southern SCS (Figure 1). The Xisha Islands are a group of atolls situated on an elevated submarine plateau, surrounded by seawater at depths over 1000 m. The submarine plateau is composed of mainly basaltic pyroclastic rocks developed at ~35.5 ± 0.9 Ma (Zhang et al., 2020), and the reefs then initiated on this basement ~19.6 Ma (Fan et al., 2020). The Nansha Islands (with ~117 reefs and ~3000 km^2 reef area) are ≥400 km away from the closest mainland. The reef strata of the Nansha Islands are over 2000 m thick, and have accumulated since the upper Oligocene (Yu and Zhao, 2009). Most corals from the Xisha and Nansha Islands used in our study are *Porites* sp.

Other coral samples used in this study, including *Acropora* sp., *Cyphastrea* sp., *Favia* sp. and *Porites* sp., were collected from Clerke Island (11º58′S, 143º17′E), Gore Island (11º59′S, 143º14′E), Haggerstone Island (12º02′S, 143º17′E), Alexandra Reef (16º31′S, 145º28′E) and High Island (17º09′S, 146º00′E) in the northern GBR, and Great Keppel Island (23º10′S, 150º59′E) in the southern GBR. Clerke, Gore and Haggerstone Islands are located in the remote Cape York Peninsula region of the far northern GBR. Coastal development of the adjacent mainland is minimal, with the majority of land use in adjacent catchments dedicated to nature conservation (~80%) (Waterhouse et al., 2016). Alexandra Reef is a largely remnant emergent Holocene mainland fringing reef dominated by large sub-fossil *Porites* sp. microatolls (diameters >2m) (Leonard et al., 2018). High Island is an inshore continental island with a leeward semi-emergent fringing reef flat comprised of numerous large *Porites* sp. microatolls which represent the Middle Holocene sea level highstand (Leonard et al., 2018). In the southern GBR, Great Keppel Island is a continental high island with modern fringing reefs to the windward and leeward. A patchy, infilled semi-emergent sub-fossil reef flat is present within a leeward embayment which has been dated to the Late Holocene (Leonard et al., 2016).

Ocean circulation in the Tropical Southwestern Pacific is complex (Fig. 1). The broad southern branch of the westward-flowing South Equatorial Current (SEC) encounters a series of islands (Fiji, Vanuatu and New Caledonia), resulting in several strong and narrow jets, including the North Vanuatu Jet (NVJ), South Vanuatu Jet (SVJ), North Caledonia Jet (NCJ) and South Caledonia Jet (SCJ) (Choukroun et al., 2010; Kessler and Cravatte, 2013; Hu et al., 2015). Upon approaching the Australian coast, the NVJ and NCJ bifurcate at ~14.5ºS and ~18ºS, respectively, into the Gulf of Papua Current (GPC) and the East Australian Current (EAC) (Kessler and Cravatte, 2013; Ridgway et al. 2018). The EAC starts at ~14.5 ºS and flows southward feeding the southern GBR, while the GPC, formed from two sources: surface NVJ at ~ 14.5°S and subsurface NCJ at ~18°S, flows northward feeding the northern GBR and the PNG coast (Ridgway et al. 2018). In brief, despite complex ocean circulation in the southwestern Pacific the waters reaching both the northern and southern GBR mainly originate from the southern branch of the SEC (Fig. 1).

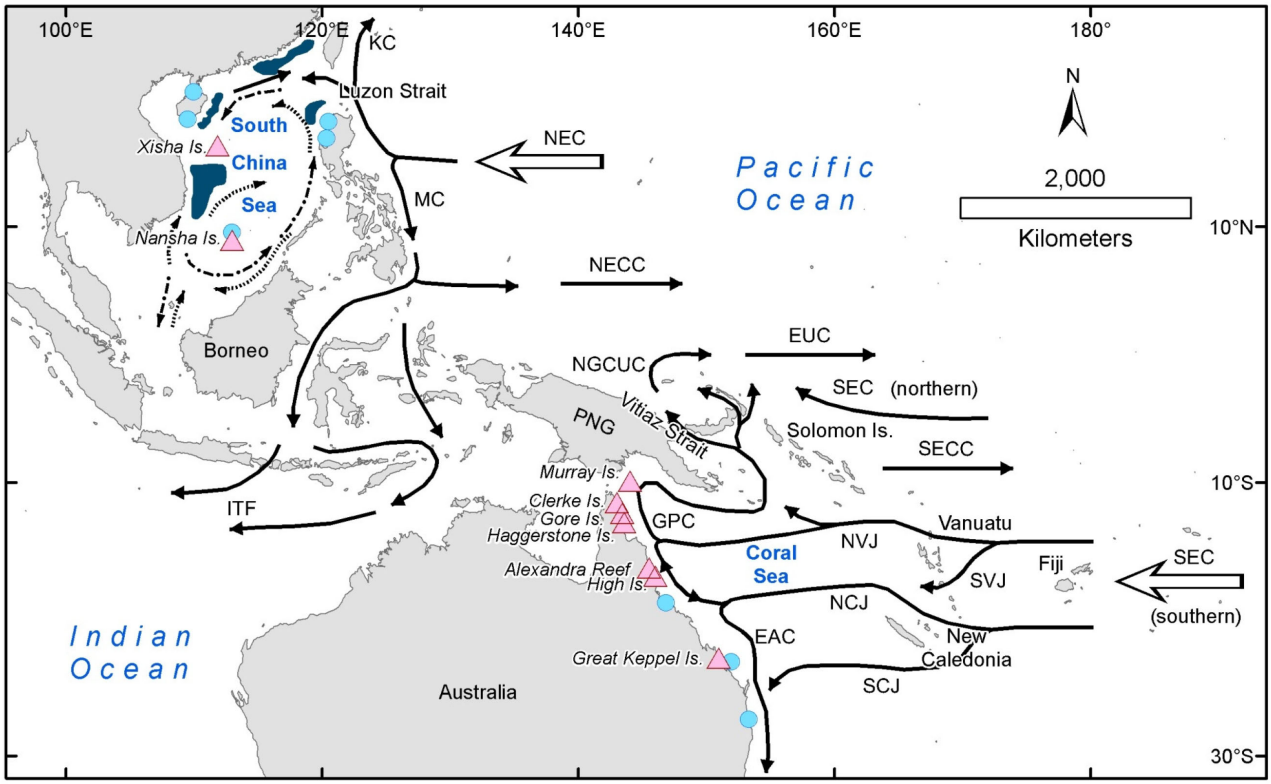

Figure 1. Map showing our study sites (pink triangles) and other sites (blue circles) from previous studies mentioned in the text, and major ocean circulation patterns. Four upwelling areas in the SCS are shown in dark cyan (Yu et al., 2010 and references therein). Ocean circulation within the SCS is after Liu et al. (2008) with dashed and dotted arrows, and dotted arrows for currents during winter and summer seasons, respectively. Other ocean circulation is after Tomczak and Godfrey (2001), Choukroun et al. (2010) and Hu et al. (2015). NEC – North Equatorial Current, KC – Kuroshio Current, MC – Mindanao Current, NECC – North Equatorial Counter Current, ITF – Indonesian Throughflow, EUC – Equatorial Undercurrent, NGCUC – New Guinea Coastal Undercurrent, SEC – South Equatorial Current, SECC – South Equatorial Counter Current, GPC – Gulf of Papua Current, NVJ – North Vanuatu Jet, SVJ – South Vanuatu Jet, NCJ – North Caledonia Jet, SCJ – South Caledonia Jet, EAC – East Australian Current.

2.2. U-Th dating

Before U-Th dating and ^{14}C analysis were carried out, corals from the SCS and the GBR were screened by Scanning Electron Microscopy (SEM) to check for possible diagenesis (Nothdurft and Webb, 2009). Screening was performed at the Queensland University of Technology using an Hitachi TM3000 Benchtop SEM with energy dispersive spectroscopy in the Central Analytical Research Facility. Pieces of the coral samples that were clean (lacking macroscopic sediment and pervasive cement in pores spaces) were cut with a diamond saw (<1 cm^3) and analysed with SEM for identifying deleterious diagenetic products (see Supplementary Fig. S1). These include porefilling cements including marine aragonite and high magnesian calcite cements, meteoric cements, and extensive bioerosion (Nothdurft and Webb, 2009; Hua et al., 2015). Samples that passed SEM screening were selected (see Supplementary Fig. S3) and crushed into chips (~1 mm diameter) and

visually inspected using a compound microscope. Individual chips that showed any evidence of microbialite, staining or cement were excluded from dating. Post-analysis screening criteria included comparing initial $\delta^{234}U$ with modern sea water values of 147 ± 5‰ (Reimer et al., 2009 and references therein) and high initial $^{230}Th/^{232}Th$ values indicating low levels of non-radiogenic ^{230}Th and high levels of detrital ^{232}Th.

Forty-four unaltered coral samples including 17 from the SCS, 21 from the northern GBR and 6 from the southern GBR were dated using the U-Th method in the Radiogenic Isotope Facility at The University of Queensland. Samples were soaked in a 10% H_2O_2-Milli-Q water solution for 24h followed by repeated sonication in Milli-Q water until the water remained clear. Samples were then dried on a hotplate at 40˚C. All the SCS coral samples were analysed before 2010 using a VG Sector-54 thermal ionization mass spectrometer (TIMS; Zhao et al., 2001). Approximately 0.5 g of each sample was spiked with a ^{229}Th–^{233}U–^{236}U mixed tracer. The samples were dated following column separation and TIMS analytical procedures as described in detail in Zhao et al. (2009) and Clark et al. (2012). The GBR coral samples were measured using a Nu Plasma multi-collector-inductively coupled plasma-mass spectrometer (MC-ICP-MS). For these analyses, ~0.15 g samples were spiked with a ^{229}Th–^{233}U mixed tracer and dated following a modified and simplified column separation procedure and a fully-automatic MC-ICP-MS measurement protocol described in detail in Zhou et al. (2011) and Clark et al. (2014). All ages were calculated with the Isoplot Program EX/3.0 of Ludwig (2003) using decay constants of Cheng et al. (2000). Typical external age reproducibility for the ^{230}Th dating, based on repeated measurements of standards, was better than 0.5% (2σ). All ^{230}Th ages obtained from the GBR were corrected using a two-component mixing equation to account for both initial sources of $^{230}Th/^{232}Th$ as in Clark et al. (2014). In this study a hydrogenous $^{230}Th/^{232}Th$ value of 1.083 ± 20% and an isochron inferred detrital $^{230}Th/^{232}Th$ value of 0.61 ± 20% was used (Clark et al. 2014).

2.3. Radiocarbon analysis

All U-Th dated corals were analysed for radiocarbon. Most of the corals encompassed 3-10 yr of growth except for the three samples from Yongshu Reef, Nansha Is. (OZM066-OZM068), which spanned only ~1 yr of growth or less (see Supplementary Table S3). The samples were cut using a diamond saw, cleaned in Milli-Q water, oven dried, and homogenised using a clean mortar and pestle.

To investigate the modern values of the MRE for the northern GBR, three known-age museum shell specimens from Murray Island (9°55′S, 144°03'E) were also analysed for radiocarbon. These samples are suspension-feeding shellfish (*Arca ventricosa* and *Atactodea striata*), which were live collected in 1907 and curated at the Australian Museum (see Supplementary Table S1). *A. ventricosa* occurs on rocks and corals in the littoral to sublittoral zone (<20 m) and *A. striata* is a shallow burrower on sandy beaches in the intertidal zone (Carpenter & Niem 1998). The shell samples were sampled at the shell margin, treated with dilute HCl to remove possible carbon contamination (e.g., secondary carbonate) then cleaned in Milli-Q water three times for 15 min each, then oven dried.

A total of 47 samples (44 coral and 3 shell samples) were converted to CO_2 by reacting with 85% H_3PO_4 then to graphite using the H_2/Fe method (Hua et al., 2001). A portion of graphite was used for the determination of $\delta^{13}C$ for isotopic fractionation correction using a Micromass IsoPrime elemental analyzer/isotope ratio mass spectrometer (EA/IRMS). Accelerator mass spectrometry (AMS) analysis

of these samples was performed using the STAR Facility at ANSTO (Fink et al., 2004), with a typical precision of ~0.3-0.4% (1σ).

3. Results

The results of U-Th dating and AMS ^{14}C analysis of 44 coral samples are presented in Supplementary Tables S2 and S3, respectively. ^{230}Th dates representing absolute ages of corals were reported in years relative to the time of measurement, and to AD 1950 or calendar years before present (cal. yr BP). The latter ages were employed for the calculation of ΔR, R and decay-corrected $\Delta^{14}C$ values as shown in Supplementary Table S3. As there is a positive correlation between ΔR and R, and a negative correlation between ΔR and $\Delta^{14}C$ (e.g., Hua et al., 2015; Komugabe-Dixson et al., 2016), we only present and discuss temporal variations in ΔR values in the text. Radiocarbon results of the three museum shell specimens collected from the northern GBR and their associated ΔR values are shown in Supplementary Table S1. ΔR for a sample was calculated using the following equation:

$$\Delta R(t) = \text{Measured } ^{14}C \text{ age}(t) - \text{Marine model } ^{14}C \text{ age}(t)$$

where t is ^{230}Th age of the sample (for corals) or the time of collection for the sample (for historical shell specimens) in cal. yr BP, and Marine model ^{14}C age at time t is from Marine13 (Reimer et al., 2013). All ΔR values and associated uncertainties were estimated using the online *deltar* software (Reimer and Reimer, 2017) (URL: http://calib.org/deltar/, date of access xxxx).

ΔR values for the SCS from the current study together with previously published values for Leizhou Peninsula, Sayna and Nansha Is. (Yu et al., 2010) and for Luzon Is. (Hirabayashi et al., 2019) are shown in Fig. 2a. The modern weighted mean ΔR value for the SCS of -22 ± 47 yr is also plotted in Fig. 2a for comparison. This value was calculated from 10 ΔR values including three values from Xisha Is. and one from Saigon (Southon et al., 2002), one from Con Dao Island (Dang et al., 2004), three from the Philippines (Southon et al., 2002), one (1950 datum) from Hon Tre Island (Bolton et al., 2016), and one (1950 datum) from Luzon Is. (Hirabayashi et al., 2019). This weighted mean value is similar to the modern weighted mean ΔR value for the SCS of -23 ± 52 yr previously employed by Yu et al. (2010), which was based on the first five ΔR values listed above.

For samples of similar ages, good agreement between the new and published ΔR values is found in most cases, particularly at ~ 0.75, 2.9, 4.0, 4.9, 5.6 and 5.8 cal. kyr BP. There are two cases where clear differences between the new and published values are observed. The first case around 5.3 cal. kyr BP is for two samples from Nansha Is., with a difference of ~120 yr. However, these two values are within 1σ range of the modern mean ΔR value, indicating that such magnitude of difference might reflect natural ΔR variability. The second case at ~2.5 cal. kyr BP involves one new datum from Nansha Is. and two published data from Leizhou Peninsula. These differences of 110-120 yr are also in the range of natural ΔR variability. These observations indicate that the coral samples shown in Fig. 2a, which are widely distributed in the SCS basin, are fed by the same water, further supporting that SCS surface water is overall well-mixed on relative short time scales as noted by Yu et al. (2010).

All SCS ΔR values, shown in Fig. 2a, vary between -106 and 391 yr during the past ~8.1 cal. kyr BP with most data being within 1σ range of the modern mean value. Substantial ΔR variability occurs during two periods, ~5.5-8.1 and ~2-3.5 cal kyr BP, with respective magnitudes of variability (from trough to peak) of ~410 yr and ~200 yr.

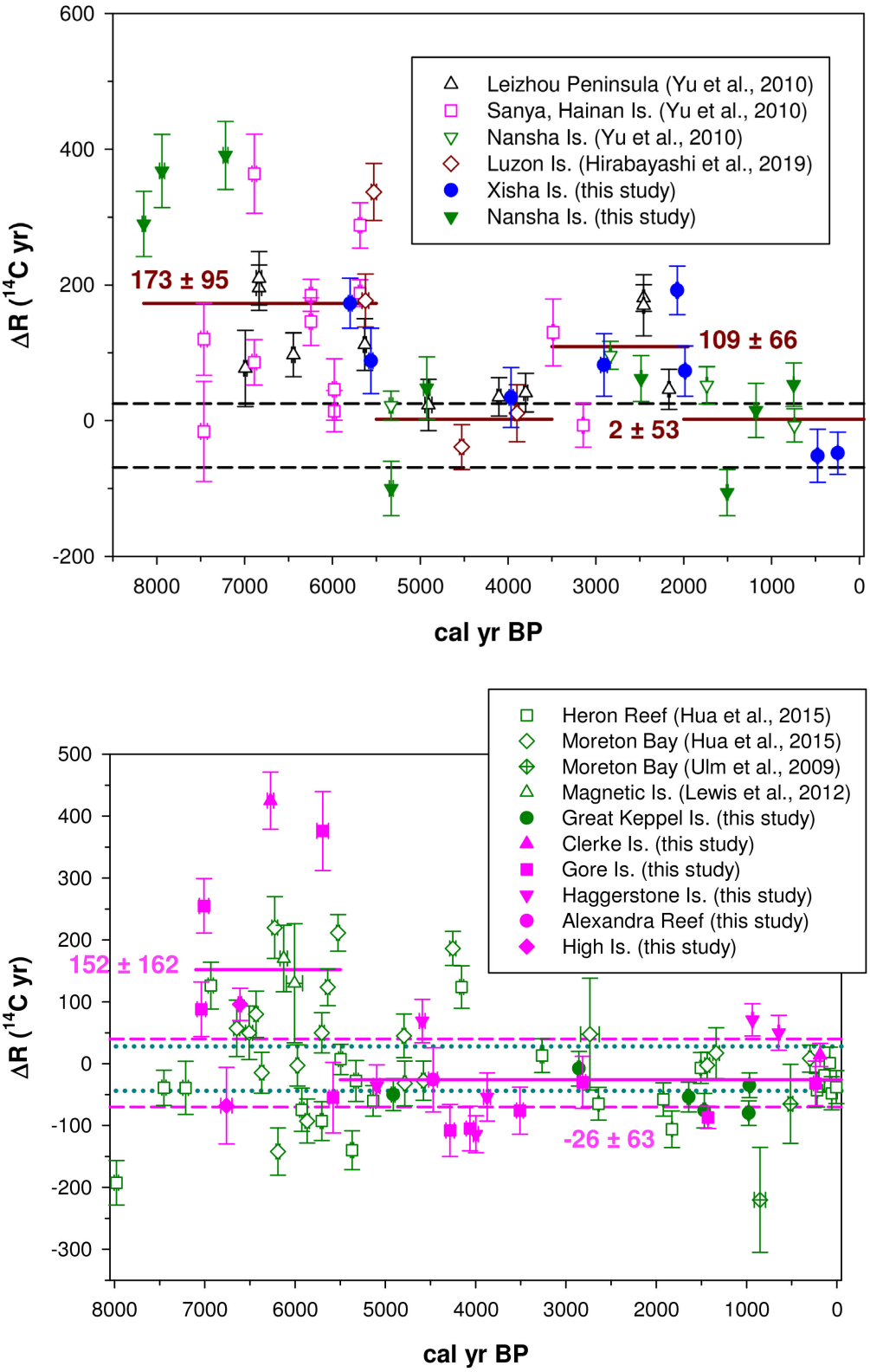

Figure 2. Temporal ΔR variations during the past ~8.1 cal.kyr BP for (a) the SCS, and (b) the northern and southern GBR. Black dashed lines depict 1σ range of modern ΔR values for the SCS. Pink dashed and green dotted lines represent 1σ range of modern ΔR values for the northern and southern GBR, respectively. Solid lines represent weighted mean ΔR values for different time periods. Vertical error bars are 1σ. Horizontal error bars are 1σ for paired terrestrial/marine samples from Ulm et al. (2009), and 2σ for corals (all other samples).

Fig. 2b shows ΔR values for the northern GBR and Great Keppel Is. in the southern GBR, together with previously published data for Heron Reef (Hua et al., 2015), Moreton Bay (Ulm et al., 2009; Hua et al., 2015) and Magnetic Is. (Lewis et al., 2012) in the southern GBR. The pre-bomb ΔR values for the northern GBR derived from the three museum shell specimens range from -70 to 30 yr (see Supplementary Table S1). The weighted modern mean ΔR value for the northern GBR of -17 ± 56 yr derived from the three museum shell specimens (see Supplementary Table S1) together with that for the southern GBR of -8 ± 36 yr (Hua et al., 2015) is also plotted in Fig. 2b for comparison.

For the period ~0-5.5 cal. kyr BP, most of the northern GBR data are within 1σ range of their modern mean value except for two data points around 4 and 0.9 cal kyr BP, which are slightly lower and higher than the range, respectively. In this period, there are three pairs of samples at similar ages but from different islands. Good agreement in ΔR values for two out of the three pairs is observed: Gore Is. and Haggerstone Is. at ~4 cal kyr BP, and Gore Is. and Clerke Is. at ~0.2 cal kyr BP. The other pair (~4.5-4.6 cal. kyr BP) for Alexandra Reef and Haggerstone Is. do not agree with each other within 1σ uncertainties. However, the two values are within the 1σ range of the modern mean value for the northern GBR, suggesting that their difference of ~100 yr might reflect natural ΔR variability. These observations indicate that the study islands and reef in the northern GBR receive the same surface water. In contrast, large ΔR variability (from trough to peak) of ~490 yr is observed for the period ~5.5-7 cal. kyr BP, in which the majority of the data is higher or much higher than their modern mean value (five out of seven values).

Most of the ΔR values (four out six values) for Great Keppel Is. spanning from ~1.0 to 4.9 cal. kyr BP are within the 1σ range of modern mean value for the southern GBR. Only two values around 1 and 1.5 cal. kyr BP are slightly lower than the modern 1σ range. These data together with those previously published for the southern GBR indicate this region experienced much less ΔR variability during the past ~5.5 cal. kyr BP compared to the Middle Holocene.

4. Discussion

4.1. Temporal ΔR variability for the South China Sea

During the Middle Holocene, large variations in SCS ΔR values are evident. Most of the ΔR values in this period are higher or much higher than their modern mean value (Fig. 2a). Our highest ΔR values are obtained from the three oldest corals from Nansha Is., each of which spans only ~1 yr of growth or less instead of 3-10 yr of growth for the other corals used in our study. An obvious question is whether these high values are due to possible large seasonal/annual variability in surface ocean ^{14}C (Druffel et al., 2001; Morimoto et al., 2004). Yu et al. (2010) compared ΔR values from seven pairs of seasonal/annual and decadal (~10 yr) SCS corals spanning ~2.5-7.5 cal. kyr BP, and reported that most of the paired samples delivered similar ΔR values, which agreed with each other within 1σ (four pairs) and 2σ (six pairs) uncertainties. This indicates that seasonal/annual variability in surface water ^{14}C is insignificant in our study and the reported high ΔR values from the three oldest Nansha Is. corals reflect their real values. These three highest values of 290-391 yr during ~7.2-8.1 cal. kyr BP are similar to the highest ΔR values reported in Yu et al. (2010) and Hirabayashi et al. (2019) (364 yr at 6.9 cal. kyr BP for a Sanya coral and 337 yr at 5.5 cal. kyr BP for a Luzon Is. coral, respectively), extending the period of large ΔR variations in the Middle Holocene to ~5.5-8.1 cal. kyr BP (Fig. 2a). Similarly, during the Late Holocene the highest new ΔR value from Xisha Is. (192 yr at ~2.1 cal. kyr BP) is similar to the highest values from Leizhou Peninsula (170-181 yr at ~2.5 cal. kyr BP) reported

in Yu et al. (2010). This new value together with another elevated value from Xisha Is. at ~2 cal. kyr BP extends the period of elevated ΔR in the Late Holocene to ~2-3.5 cal. kyr BP (Fig. 2a). All the SCS data clearly show large temporal ΔR variations of ~410 yr during the Middle Holocene and smaller ΔR variability of ~200 yr during the Late Holocene.

Surface waters reaching the SCS are mainly from the KC, which originates from the NEC (Fig. 1). Thus, the ^{14}C content of SCS surface waters is related to the ^{14}C level of the NEC and its contribution to the SCS. Radiocarbon content of the NEC is influenced by ENSO variability and associated changes in ocean circulation. During La Niña events, ocean upwelling in the Tropical East Pacific (TEP) is enhanced bringing ^{14}C-depleted subsurface waters to the surface. These old surface waters are possibly spread to the Tropical West Pacific (TWP) by the NEC and SEC (Hua et al., 2015). More frequent/stronger ocean upwelling along the equator associated with enhanced easterly winds under La Niña conditions results in low ^{14}C level for equatorial surface waters, which are also contributed to the NEC (Yu et al., 2010 and references therein). In contrast, ocean upwelling in the TEP and along the equator Pacific is significantly reduced during El Niño events, leading to higher ^{14}C level (or lower ΔR value) for the NEC during El Niño conditions compared to that during La Niña conditions. In addition, ENSO variability influences the NEC bifurcation latitude, KC strength and the Kuroshio intrusion into the SCS known as the Luzon Strait transport (LST) (Hu et al., 2015; Nan et al., 2015). The KC (~15 Sv between ~10-23°N) is stronger/weaker during La Niña/El Niño events (Qiu et al., 2019), leading to lower/higher LST (3-6.5 Sv) from the Pacific into the SCS (Nan et al., 2015). As a result, during La Niña years ^{14}C-depleted waters from the NEC enters the SCS although the LST is reduced, leading to higher SCS ΔR values compared to those during El Niño years.

Ocean upwelling within the SCS basin also affects its ΔR values. Ocean circulation in the SCS is mainly driven by monsoon winds, resulting in a basin-wide cyclonic gyre during winter, and a strong anticyclonic gyre in the southern basin and a weaker cyclonic gyre in the northern basin during summer, with a few stable oceanic eddies (Fig. 1) (Hu et al., 2000; Liu et al., 2008). The Kuroshio intrusion also generates oceanic eddies around the Luzon Strait, mostly during winter (Nan et al., 2015; Qiu et al., 2019). According to Hong et al. (2009), coastal upwelling along the Taiwan Strait is associated with the Asian monsoons. This coastal upwelling together with the above oceanic eddies form four regions of ocean upwelling in the SCS as shown as shaded areas in Fig. 1. Such ocean upwelling, bringing old subsurface waters to the surface leading to higher SCS ΔR values, is positively correlated with East Asian Monsoons (Yu et al., 2010; Hirayabashi et al., 2019).

Possible mechanisms for elevated SCS ΔR values during the Middle Holocene include (i) substantially low ^{14}C level for surface waters in the TEP as a result of not only higher/stronger ocean upwelling in this region associated with higher/stronger La Niña activity or lower ENSO variability (Fig.3; Yu et al., 2010; Hirabayashi et al., 2019) but also a higher contribution of old Subantarctic Mode Water (SAMW) (Hua et al., 2015) and/or old Antarctic Intermediate Water (AAIW) (Carré et al., 2016) to the upwelled waters. This together with increased westward advection of old and saltier waters from the TEP to the TWP by the NEC (Hua et al., 2015 and references therein), carries ^{14}C-depleted waters to the SCS, (ii) increased contribution of ^{14}C-depleted equatorial surface waters to the NEC under La Niña conditions and consequently to the SCS, and (iii) enhanced East Asian Monsoons bringing ^{14}C-depleted subsurface waters in the SCS to the surface (Fig. 3; Yu et al., 2010; Hirabayashi et al., 2019). It is worth noting that although there is no clear consensus on ENSO variability, most proxy records and model simulations indicate an overall strengthening of ENSO from Early to Late Holocene (Fig. 3; Moy et al., 2002; Conroy et al., 2008; McGregor et al., 2013; Liu et al., 2014; Discroll et al., 2014).

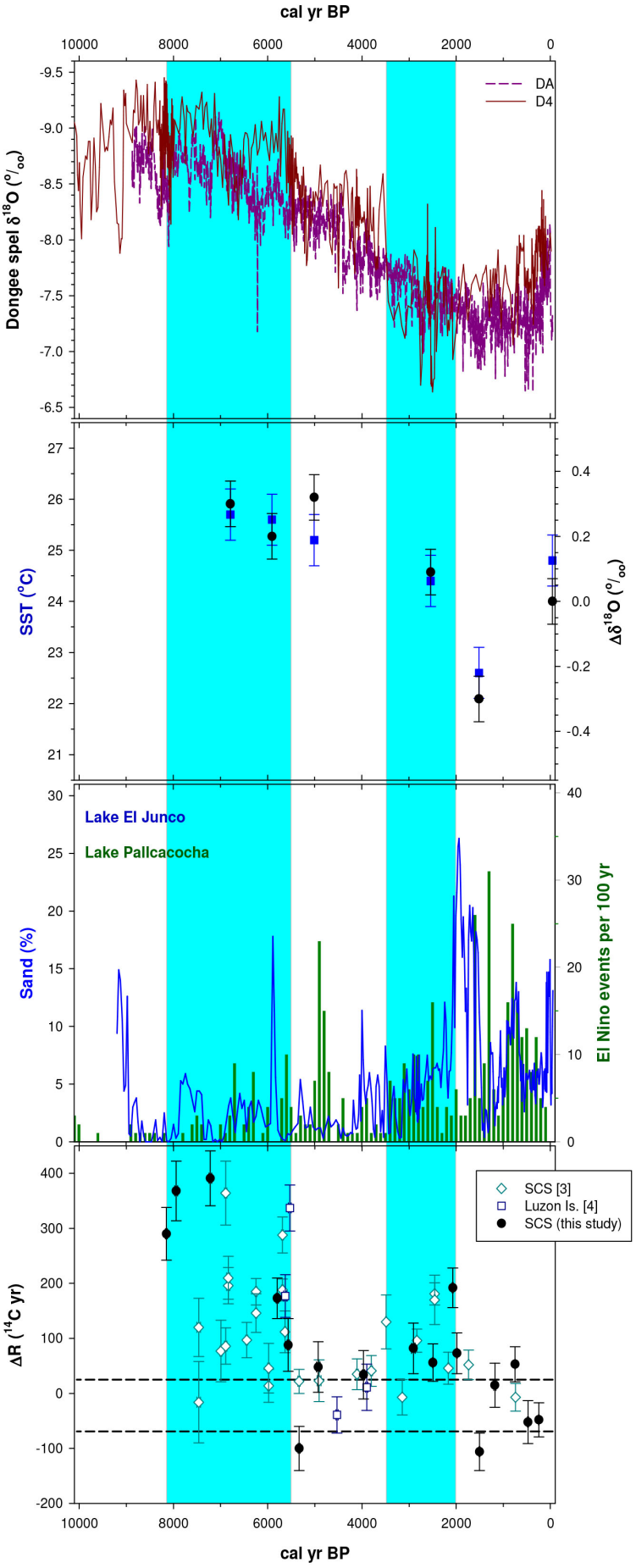
cal yr BP
10000
8000
6000
4000
2000
0
Dongee spel δ18O (‰)
DA
D4
SST (°C)
Δδ18O (‰)
Lake El Junco
Lake Pallcacocha
Sand (%)
El Nino events per 100 yr
SCS [3]
Luzon Is. [4]
SCS (this study)
ΔR (14C yr)
cal yr BP
+
EASM
−
+
ENSO
−

Figure 3. Climate records vs SCS ΔR values during the Holocene. The light blue shaded areas represent periods of large ΔR variations for the SCS (~5.5-8.1 and ~2-3.5 cal. kyr BP). Sources of published ΔR values are [3] Yu et al. (2010) and [4] Hirabayashi et al. (2019). Sources of climatic records are Moy et al. (2002) for Lake Pallcacocha record, Conroy et al. (2008) for Lake El Junco record, Dykoski et al. (2005) for $\delta^{18}O$ in D4 stalagmite, Wang et al. (2005) for $\delta^{18}O$ in DA stalagmite, and Yu et al. (2005) for coral-based SST and relative salinity ($\Delta\delta^{18}O$) of the SCS. Elevated SST and $\Delta\delta^{18}O$, reflecting more saline seawater due to transportation of more moisture out of the tropics, indicate strong EASM (Yu et al., 2005).

During the period ~2-3.5 cal. kyr BP in the Late Holocene, the coral-based SST and relative salinity ($\Delta\delta^{18}O$) records suggest a relatively stronger East Asian Summer Monsoon (EASM; Fig. 3). This is supported by Chinese historic documents suggesting much wetter and warmer conditions for China from ~2.5-2.8 kyr ago and by coral proxies in the southern SCS indicating relatively storminess in this region from 2.2-3.3 cal. kyr BP (Yu et al. 2010 and references therein). However, the Dongee stalagmite $\delta^{18}O$ records do not suggest relatively stronger EASM during the 2-3.5 cal. kyr BP interval although there are large $\delta^{18}O$ variations in the D4 stalagmite during this period (Fig. 3). According to Yu et al. (2010) this period saw discrepancies among various stalagmite $\delta^{18}O$ records from sites surrounding the SCS, possibly due to competing factors influencing the stalagmite $\delta^{18}O$ signals. The period ~2-3.5 cal. kyr BP experienced slightly higher ENSO activity than previous periods, but much lower than more recent periods. There was a significant increase in rainfall events recorded in Galapagos lake El Junco after ~2 cal. kyr BP associated with increased ENSO activity (Fig. 3). Higher ΔR values during ~2-3.5 cal. kyr BP might be due to the combination of relatively higher EASM and relatively lower ENSO activity.

4.2. Temporal ΔR variability for the Great Barrier Reef

Large ΔR variations similar to those observed in the SCS are also evident during the Middle Holocene in the northern GBR. Three samples (OZU736, OZU732 and OZU734) of ~7.0, 6.3 and 5.7 cal. kyr BP, respectively, delivered much higher ΔR values than their modern mean value (Fig. 2b). New materials from these three coral samples together with that from sample OZU745 of ~6.6 cal. kyr BP were collected for duplicate analyses including SEM screening, U-Th dating and AMS ^{14}C measurement. The duplicate results (U-Th and ^{14}C ages) for these samples are similar to their original values, with most of the ^{230}Th ages agreeing with each other within 2σ uncertainties and all ^{14}C ages in concordance with each other within 1σ uncertainties (see Supplementary Tables S2-S3). This indicates that ΔR values derived from these four samples are accurate and not a result of diagenesis or analytical problems.

It is interesting that the timing of the three high ΔR values (~7.0, 6.3 and 5.7 cal. kyr BP) for the northern GBR mentioned above is similar to the timing of high values observed for the southern GBR (~7.0, 6.2 and 5.6 cal. kyr BP; Fig. 2b), with the former values (255-425 yr) being 160 yr on average higher than the latter (125-220 yr). In addition, the magnitude of ΔR variations for the northern GBR is ~490 yr from peak to trough, which is similar to that of ~410 yr for the southern GBR (Hua et al., 2015). However, the southern GBR sees both positive and negative ΔR anomalies (higher and lower than the modern mean value, respectively) with similar magnitudes, while the northern GBR experiences only positive ΔR anomalies. Similar timing and magnitudes of ΔR variations throughout

the GBR, together with the same source of surface waters reaching these regions (the southern branch of SEC), might suggest that local/regional effects are responsible for elevated positive ΔR anomalies and the lack of negative ΔR anomalies, or more ^{14}C-depleted surface waters in the northern GBR (compared to the southern GBR).

Toth et al. (2017) investigated temporal ΔR variations derived from corals from the Florida Keys reef tract during the Holocene and reported that ΔR values for nearshore reefs (<100 km from mainland Florida) were ~100 yr on average higher than those for open ocean sites (>100 km from mainland Florida) during the period ~5-8 cal. kyr BP. The authors argued that as a result of lower sea level (~7-11 m below the present sea level at ~7-8 cal. kyr BP) the distance between the reefs and shore was smaller and transmissivity of groundwater through the carbonate geology of South Florida would increase, leading to more contribution of ^{14}C-depleted submarine groundwater to the nearshore reefs and consequently higher ΔR values. Based on Toth et al. (2017), the high ΔR values observed during the period ~5.5-7 cal. kyr BP could partly be due to contribution of old submarine groundwater. Our study sites in the northern GBR are nearshore sites ~2-15 km from the coast. Eastern Queensland experienced a wet climate during the Middle Holocene (Reeves et al., 2013), which would allow a higher contribution of groundwater to the study sites. $\delta^{13}C$ of groundwater dissolved inorganic carbon (DIC) is dependent on the geology of the groundwater aquifers. Groundwater DIC $\delta^{13}C$ values are in a range of -9.4 to -17.8‰ and -2.2 to -11.4‰ for a sandstone aquifer in the West Canning Basin in Western Australia (Meredith et al., 2018) and a coastal limestone aquifer in Rottnest Island off the coast of Perth in Western Australia (Bryan et al., 2017), respectively. $\delta^{13}C$ and ^{14}C data of groundwater DIC in northeastern Queensland are scarce, and the main geology of this region is Jurassic sediments, predominantly in sandstone and siltstone (Turner et al., 2009) and Early Paleozoic, fairly deep-marine quartz-rich sandstone and mudstone intercalated with submarine mafic and felsic volcanic rocks (Jell, 2013). We therefore use groundwater DIC $\delta^{13}C$ of -10.6 to -18.4‰ from a sandstone aquifer in the Burdekin River delta near Townsville in northeastern Queensland (Fass et al., 2007) as a representative range of DIC $\delta^{13}C$ for northeastern Australia. If submarine groundwater contributed to our study sites, we would see higher negative $\delta^{13}C$ values for our corals compared to the typical $\delta^{13}C$ range of -4 to 4‰ for corals (Stuiver and Polach, 1977). However, this is not the case as our measured coral $\delta^{13}C$ values during this period range from -1.0 to -2.6‰ (see Supplementary Table S3), which is in the range for marine samples. Moreover, the global fresh groundwater sipping into the ocean is 2.2-2.4 x 10^{12} m^3 yr^{-1} or 0.07-0.08 Sv (Moore, 2010 and references therein). Regional groundwater sipping into the ocean along the northern Queensland coast, which is much lower than 0.07-0.08 Sv, is too small compared to the strength of the GPC of 12-25 Sv (Kessler and Cravatte, 2013). These factors together with a high sea level along the Queensland coast during the period of 5.5-7 cal. kyr BP (similar or ~1-2 m higher than the present sea level; Lewis et al., 2013; Leonard et al., 2016, 2018) rather than a lower sea level as in the study of Toth et al. (2017), indicate that the groundwater effect might be likely negligible for our study sites.

Hua and colleagues (2015) proposed a possible mechanism for large ΔR variations observed in the southern GBR during the Middle Holocene. They attributed these ΔR changes to variability in ocean circulation associated with climate change, such as La Niña/El Niño conditions, intensity of easterly trade winds, positions of the Intertropical Convergence Zone (ITCZ) and the South Pacific Convergence Zone (SPCZ), which controlled the spread of old surface waters from the TEP to the west. The authors argued that during Middle Holocene La Niña conditions, limited old surface waters in the TEP were transported to the TWP by the SEC due to a strengthened Salinity Front (see Fig. 4). During La Niña events, the southern branch of the SEC moved northward and its ^{14}C content was higher resulting from enhanced air-sea gas exchange in association with strengthened easterly winds.

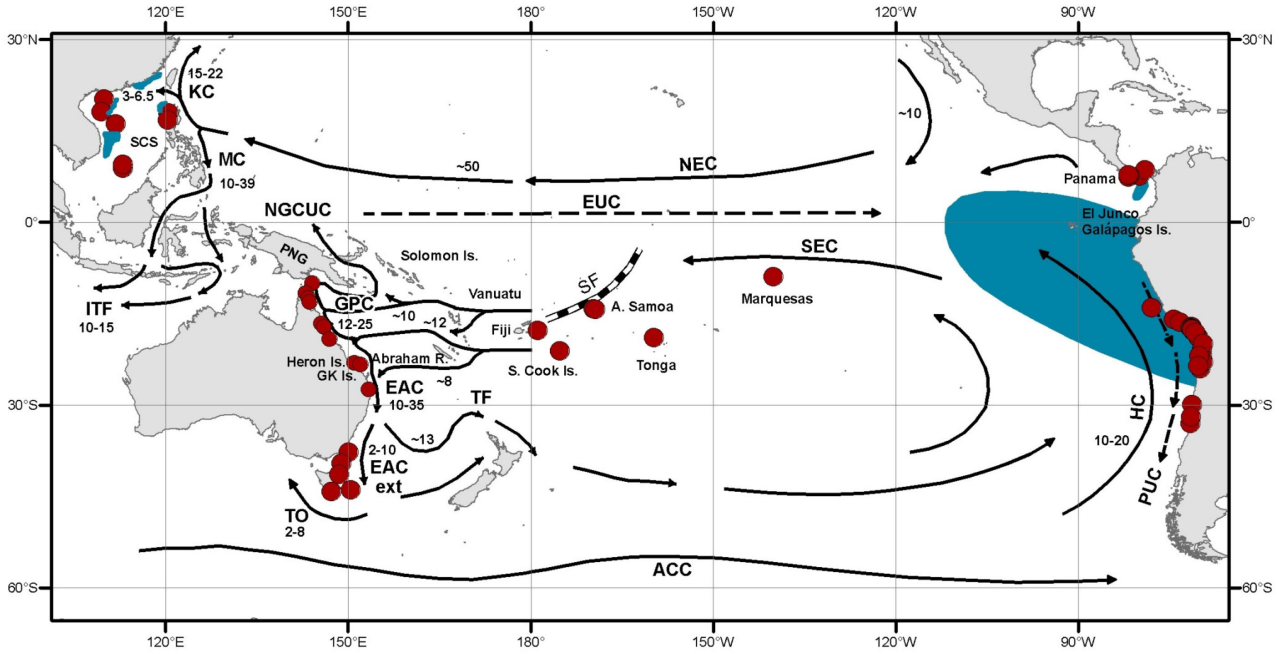

Figure 4. Map of the Tropical and South Pacific showing major ocean circulation patterns and ΔR sites. Ocean circulation is after Tomczak and Godfrey (2001), Ridgway and Dunn (2003) and Hu et al. (2015). Dark cyan areas represent major upwelling regions. NEC – North Equatorial Current, KC – Kuroshio Current, MC – Mindanao Current, ITF – Indonesian Throughflow, EUC – Equatorial Undercurrent, NGCUC – New Guinea Coastal Undercurrent, SEC – South Equatorial Current, GPC – Gulf of Papua Current, EAC – East Australian Current, EAC ext. – EAC extension, TF – Tasman Front, TO – Tasman Outflow, ACC – Antarctic Circumpolar Current, HC – Humboldt Current, PUC – Peruvian Under Current, SF – Salinity Front. Number next to an ocean current represents either its range or mean of geostrophic volume transport in Sverdrup (Sv; 1Sv = 10^6 m^3 s^{-1}) taken from Tilburg et al. (2001), Middleton and Cirano (2005), Checkley and Barth (2009), Talley et al. (2011); Kessler and Cravatte (2013), Hu et al., (2015); Nan et al. (2015) and Qiu et al. (2019).

These factors led to negative ΔR anomalies for the southern GBR. In contrast, possible higher/stronger El Niño activity during ~5.4-7 cal. kyr BP allowed increased transportation of old surface waters to the west due to a weaker Salinity Front and resulted in a more southward position of the equatorial branch of the SEC containing ^{14}C-depleted waters. These old waters reached the southern GBR, resulting in positive ΔR anomalies (Hua et al., 2015 and references therein). For the northern GBR, its elevated ΔR values (compared to those for the southern GBR) during the Middle Holocene can be achieved by vertical mixing between surface waters and ^{14}C-depleted sub-surface waters and/or by changes in horizontal advection bringing old surface waters to this region. Guilderson et al. (2004) reported low Δ^{14}C values associated with El Niño years in recent corals in the Solomon Sea. Similarly, Druffel and Griffins (1993, 1999) observed low Δ^{14}C anomalies associated with strong El Niño events in southern GBR corals during the 16th-19th centuries. These authors attributed these observed low coral Δ^{14}C values to changes in horizontal advection in the southwestern Pacific resulting in contribution of the equatorial branch of the SEC to the Solomon Sea and the Coral Sea during El Niño years, respectively. Such a southward shift of the equatorial branch of the SEC containing ^{14}C-depleted waters during El Niño events during the Middle Holocene might result in a

greater contribution of this SEC branch to the northern GBR (compared to the southern GBR), leading to more positive ΔR anomalies for the northern GBR. During the Middle Holocene, increased boreal summer warming over mid-latitudes in the Northern Hemisphere strengthened the Walker circulation and equatorial Pacific easterly winds, resulting in La Niña-like conditions (McGregor et al., 2013 and references therein). We speculate that such strengthened easterly winds in the TWP might increase ocean upwelling along the coast of the northern GBR, bringing old subsurface waters to the surface around 5.6 and 6.8 cal. kyr BP. This, in combination with higher ^{14}C content of the southern branch of SEC due to enhanced air-sea gas exchange during this period, could result in the observed negligible ΔR anomalies for the northern GBR during La Niña conditions as these effects drive ΔR values in different directions.

4.3. ΔR variations for the wider Pacific

4.3.1. Eastern Pacific

In the TEP, ^{14}C-depleted equatorial subsurface water (ESSW), which is mainly derived from the eastward flowing Equatorial Under Current (EUC), is brought to the surface by ocean upwelling. ESSW is carried southward by the Peruvian Under Current (PUC), feeding upwelling along the coast of Peru and Chile (Fig. 4). These coastal areas are also fed by a surface current, the equatorward-flowing Humboldt Current (HC) or Peruvian Current, bringing Subantarctic Surface Water (SSW) northward. During the Early to Middle Holocene, higher/stronger upwelling in the TEP and southeast Pacific under La Niña conditions and more contribution of old SAMW and/or AAIW to the ESSW, result in high to very high ΔR values for southern Peru – northern Chile (Hua et al., 2015; Carré et al., 2016). In contrast, ΔR values for central Chile (~32°S) are quite low during this period, indicating reduced upwelling in this region or upwelling of ventilated waters implying that old ESSW did not reach central Chile (Carré et al., 2016). ΔR values for these two regions during the Holocene (Ortlieb et al., 2011, Carré et al., 2016; Merino-Campos et al., 2019), show very different values between ~7-10 cal. kyr BP (464 ± 270 yr on average for southern Peru – northern Chile vs 28 ± 119 yr on average for central Chile) and similar values during the past ~3 cal. kyr BP (217 ± 125 yr on average for southern Peru – northern Chile vs 137 ± 72 yr on average for central Chile; Fig. 5a). The latitudinal ΔR difference observed during the Early to Middle Holocene indicates changes in the Humboldt Current system leading to a more northward position of the oceanic front between ESSW and SSW (<32°S) during this period compared to that of ~ 36.5°S during the Late Holocene (Carré et al., 2016). Although the timing is not similar, a more northward position of the Tasman Front (part of the EAC separating from the east Australian coast and flowing eastward; see Fig. 4) in the southwestern Pacific before the onset of the Holocene was reported by Bostock et al. (2006). Based on $\delta^{18}O$ in foraminifera from four deep-sea cores along the EAC path, the authors suggested the latitude of the Tasman Front was at ~26°S before ~11-12 cal. kyr BP, then moved southward after this time and reached its present latitude of ~34°S around 5 cal. kyr BP, which marks the onset of the modern EAC. According to Bostock et al. (2006), this large latitudinal shift in the Tasman Front most likely reflects responses of the ocean to changes in the Pacific wind stress curl as a result of changes in the position or strength of the equatorial trade winds and the Southern Hemisphere westerlies. Similarly, the large latitudinal change in the oceanic front between ESSW and SSW in southeastern Pacific might likely require large-scale changes in the Pacific ocean-atmosphere system leading to changes in the Humboldt Current system.

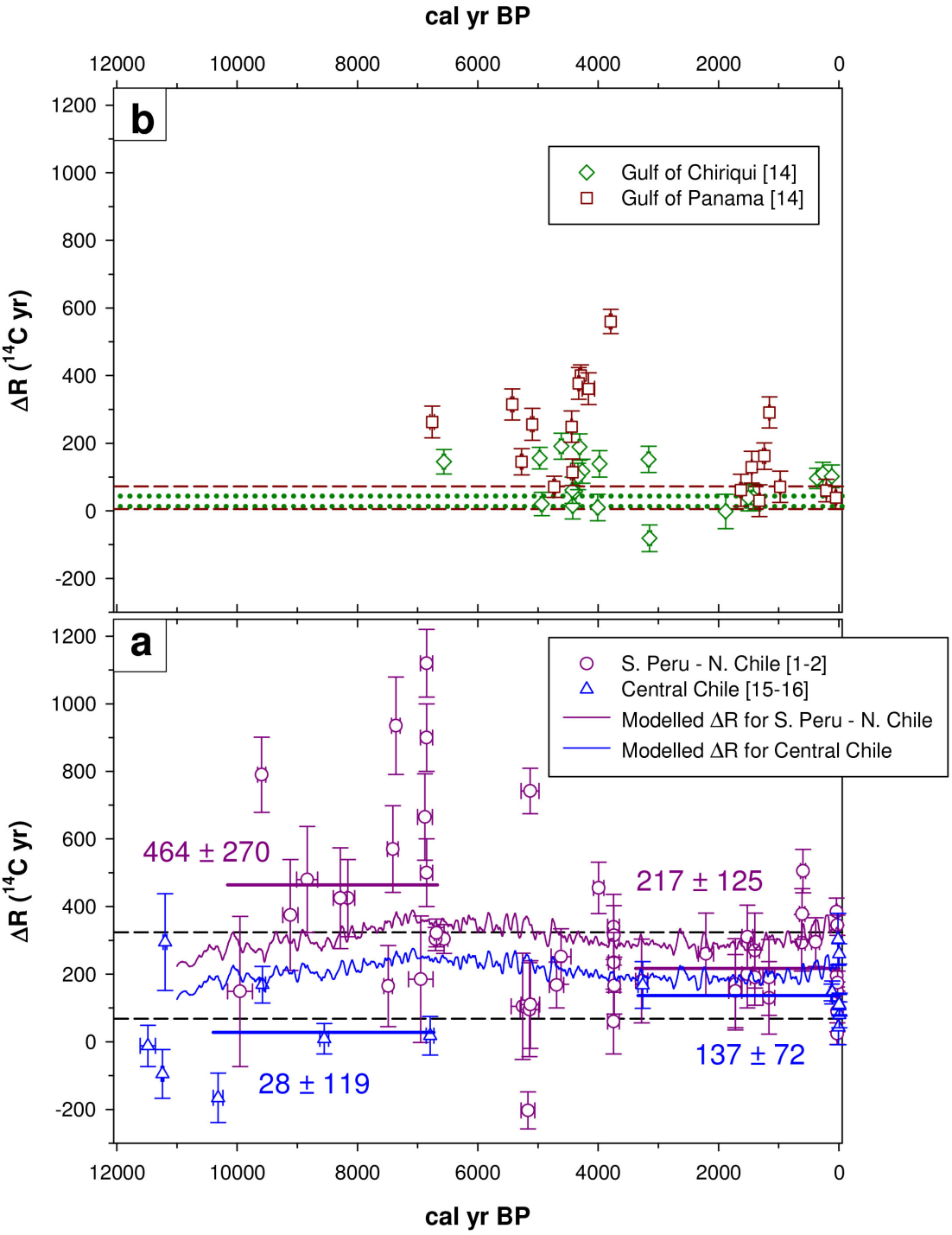

Figure 5. Temporal ΔR variability in the eastern Pacific during the past 12 cal. kyr BP. (a) southern Peru – northern Chile ([1] Ortlieb et al., 2011; [2] Latorre et al., 2017) and Central Chile ([15] Carré et al., 2016; [16] Merino-Campos et al., 2019). Solid thick lines represent weighted mean ΔR values for different time periods. Solid thin lines depict temporal variability in modelled ΔR values derived from Butzin et al. (2017) and Alves et al. (2019). Dashed lines represent 1σ range of the modern ΔR values for southern Peru – northern Chile. (b) Gulf of Panama and Gulf of Chiriqui ([14] Toth et al., 2015). Dashed and dotted lines depict 1σ range of modern ΔR values for the Gulf of Panama and the Gulf of Chiriqui, respectively. Vertical error bars are 1σ. Horizontal error bars are 1σ for paired terrestrial/marine samples ([1-2 & 15-16]), and 2σ for corals ([14], but they are too small to be seen).

Temporal ΔR variations during the Holocene were also reported for the Gulf of Panama in southern Central America, which reflect variability in ocean upwelling (Toth et al., 2015). In general, a southward ITCZ position, resulting in strengthened northeast trade winds, and low ENSO activity lead to strong upwelling in the Gulf of Panama. This explains why the highest ΔR values for the Gulf of Panama of 400-560 yr are observed during ~3.8-4.3 cal. kyr BP in the Late Holocene (Fig. 5b), which experiences a southward shift in the ITCZ position and a relatively low ENSO activity (see Fig. 3). Differences in magnitudes of large ΔR changes and in their timing between the Gulf of Panama and southern Peru – northern Chile (~500 yr at ~3.8-4.7 cal. kyr BP, ~260 yr at ~1.3-1.6 cal. kyr BP for the former region vs ~920 yr at ~6.7-7 cal. kyr BP, ~650 yr at ~5.1-5.2 cal. kyr BP for the latter region; see Figs. 5a-b) suggest that the two upwelling systems are not connected. The upwelling in the Gulf of Panama is local in size because its upwelled waters do not reach the nearby Gulf of Chiriquí, resulting in almost no substantial temporal ΔR variability for this gulf during the Holocene (Fig. 5b; Toth et al., 2015). These data indicate that old upwelled waters in the Gulf of Panama do not join those in the TEP to be spread to the TWP by the NEC and SEC (see Fig. 4). In brief, ΔR variations of ~300-1000 yr (from trough to peak) observed for coastal areas along the eastern Pacific during the Holocene are mainly due to variability in ocean upwelling associated with climate change and/or changes in the source of upwelled waters with different ^{14}C levels.

4.3.2. Across the Tropical Pacific

Large ΔR variations of several hundred to a thousand years with possible decadal/centennial fluctuations characterise the tropical Pacific during the Middle Holocene (Fig. 6). Although local/regional effects (e.g., changes in local upwelling and/or horizontal advection) partly contribute to the observed ΔR changes (e.g., the SCS and the northern GBR, as discussed previously), these ΔR variations might reflect changes in ^{14}C content of the upwelled waters in the TEP (variability in the magnitude and frequency of the upwelling, and in the contribution of SAMW and/or AAIW), variability in the contribution old waters along the equator resulting from equatorial upwelling to the east-west transport, and variability in Pacific-wide ocean circulation which controls the spread of these old surface waters in the TEP and along the equator to the TWP (see Fig. 4) as proposed by Hua et al. (2015). Our data in this study and recent published data for Vanuatu (Burr et al., 2015), showing similar magnitudes of ΔR variations in the western Pacific (~410 yr (from trough to peak) for the SCS, ~520 yr for Vanuatu, ~490 yr for the northern GBR and ~410 yr for the southern GBR), support the proposed mechanisms. Larger magnitudes of ΔR variations of ~640 yr for PNG and ~820 yr for Solomon Is. (Fig. 4) are likely due to substantial contribution of local effects such as changes in local ocean upwelling (McGregor et al., 2008; Petchey and Ulm, 2012; Hua et al., 2015). It is worth noting that there is a highly negative ΔR value of -203 yr at 5.2 cal. kyr BP in northern Chile reported in Latorre et al. (2017). This ΔR is very different than the other published values for this region (Ortlieb et al., 2011; Latorre et al., 2017), which are positive or highly positive (see Fig. 6). More ΔR values in northern Chile around this time are therefore required to see whether this highly negative ΔR is real.

The time window of these ΔR changes was estimated as ~5.4-8 cal. kyr BP by Hua et al. (2015). However, with a recently published high ΔR value of 759 yr at ~5.1 cal. kyr BP for northern Chile (Latorre et al., 2017) this period is extended to ~5-8 cal. kyr BP. Most of our elevated SCS ΔR values during the Middle Holocene are within the extended period (Fig. 6). Our oldest coral sample at ~8.1 cal. kyr BP with an elevated ΔR of ~290 yr sits marginally outside this extended period (Fig. 6). Around this time, two ΔR values currently available for southern Peru – northern Chile are similar to the 1σ range of their modern mean value. More data from southern Peru – northern Chile are required to evaluate whether there are large ΔR variations with short-term fluctuations around this time as seen at ~7 and 7.5 cal. kyr BP (Fig. 6) to increase our understanding of the mechanisms responsible for the elevated SCS ΔR value at ~8.1 cal. kyr BP.

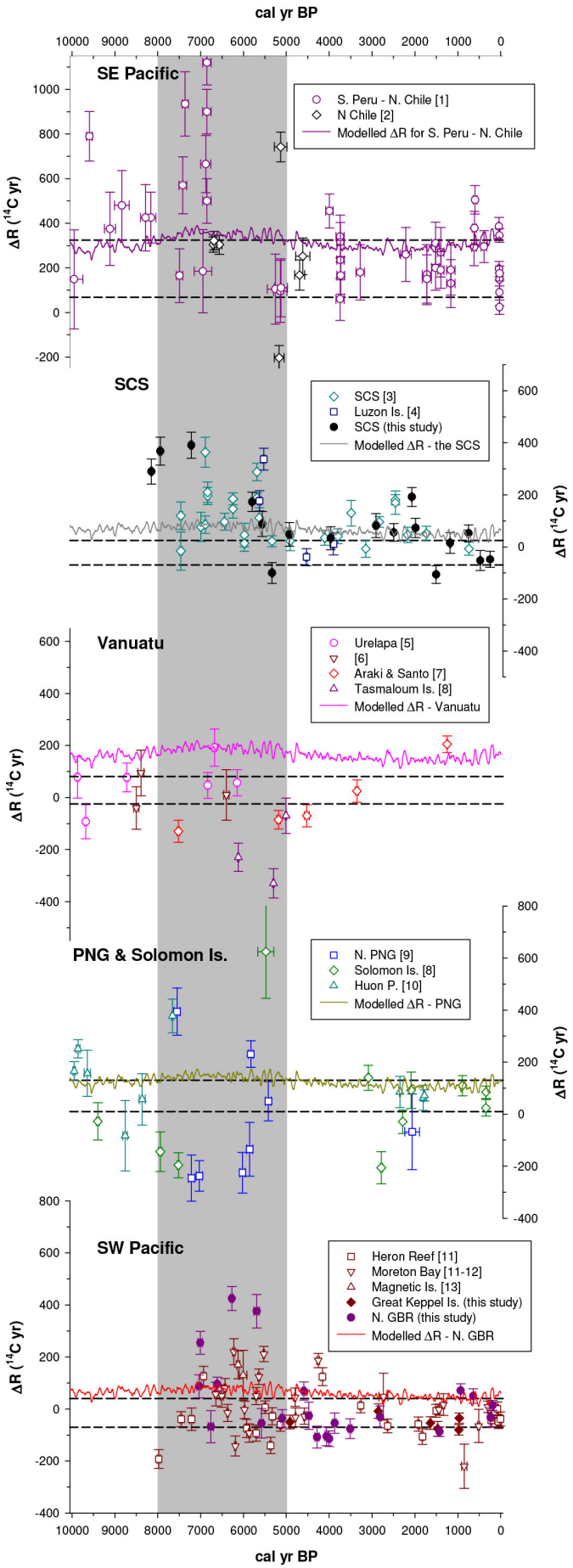

Figure 6. ΔR values for the SCS and the northern and southern GBR (SW Pacific) vs values previously published for the Tropical and South Pacific during the past 10 cal. kyr BP. For each location or region, dashed lines depict 1σ range of its modern ΔR value (see Hua et al. (2015) for modern values ΔR for southern Peru – northern Chile, Vanuatu and PNG). For the southwest Pacific, dashed lines represent 1σ ranges of the modern value for the northern GBR. Solid lines depict temporal variability in modelled ΔR values derived from Butzin et al. (2017) and Alves et al. (2019). Sources of published ΔR values are [1] Ortlieb et al. (2011), [2] Latorre et al. (2017), [3] Yu et al. (2010), [4] Hirabayashi et al. (2019), [5] Cutler et al. (2004), [6] Paterne et al. (2004), [7] Fairbanks et al. (2005), [8] Burr et al. (2015), [9] McGregor et al. (2008), [10] Edwards et al. (1993), [11] Hua et al. (2015), [12] Ulm et al. (2009) and [13] Lewis et al. (2012). Vertical error bars are 1σ. Horizontal error bars are 1σ for paired terrestrial/marine samples ([1-2, 12]), and 2σ for corals (all other samples). The grey shading for the period ~5-8 cal. kyr BP represents the timing of large variations in ΔR values across the Pacific.

4.3.3. Southwestern Pacific and South Pacific gyre

During the Late Holocene, our data show reduced ΔR variability for the northern and southern GBR as most of the values are within 1σ range of their modern mean ΔR values. Komugabe-Dixson et al. (2016) reported ΔR variations for the South Tasman during the past ~4.5 cal. kyr BP (Fig. 7), showing small negative (~250 yr) and positive (~180 yr) ΔR anomalies for the periods ~1.9-4 cal. kyr BP and 1610-1860 AD (or 90-340 cal. yr BP) during the late Little Ice Age (LIA), respectively. Recently, Petchey (2020) constructed ΔR variability for the South Pacific gyre during the past ~3.5 cal. kyr BP. Petchey (2020) found a ΔR decrease of ~200 yr in the South Pacific Gyre between 2600 and 2250 cal. yr BP, which was linked to changes in ocean circulation and climate. The majority of the ΔR values used for this construction are from the South Tasman reported in Komugabe-Dixson et al. (2016) and the remaining values are from the sites along the path of the gyre, including Marquesas, Tonga, American Samoa, southern Cook Is., Fiji and Heron Reef (see Fig. 4). Flowing southward along the east Australian coast, the EAC occurs along the western edge of the South Pacific gyre. A portion of the EAC veers eastward across the Tasman Sea as the Tasman Front (TF) at ~34°S then joins the South Pacific gyre, and the residual EAC continues flowing southward as the EAC extension along the Tasman coast before turning westward into the Indian Ocean as the Tasman Outflow (Fig. 4; Hu et al., 2015). There is a weaker eastward surface flow at ~40-41°S (compared to the Tasman Front) from the north Tasman coast toward New Zealand's coast (Ridgway and Dunn, 2003). According to Komugabe-Dixson et al. (2016) and references therein, surface waters reaching the South Tasman sites are the southward EAC extension containing ^{14}C-enriched waters and the northward ^{14}C-depleted sub-Antarctic waters from the Subtropical Front (STF), and ΔR changes at these sites reflect variations in the contribution of these two source waters given both EAC and STF have large variabilities at different timescales (e.g., seasonal, interannual and decadal). As these South Tasman sites (~37-44°S) are located south of the TF (~34°S), the main component of the southern end of the South Pacific gyre, only a small portion of the ^{14}C signal of these sites might be incorporated into the gyre through the weak eastward flow at ~40-41°S across the Tasman Sea, which varies depending on intensities of both the EAC and eastward flow. We thus compare ΔR values for the northern and western ends of the gyre, representing ^{14}C levels of the broad southern branch of the SEC and EAC and consequently the gyre, with those for the South Tasman sites as shown in the middle and bottom panels of Fig. 7, respectively.

The ΔR values for sites along the path of the gyre together with those from the southern GBR including Abraham Reef (Druffel and Griffin, 1993, 1999) and Great Keppel Is. from this study are plotted in Fig. 7 middle panel. Two periods that both data sets are sufficient for comprehensive comparison are the past ~0.3-0.4 and ~1.8-2.8 cal. kyr BP. Positive ΔR anomalies are evident in both data sets (the gyre and South Tasman sites) for the past ~340 cal. yr BP. During the late LIA (90-340 cal. yr BP), the gyre ΔR value of 10 ± 40 yr on average (ranging from -99 to 127 yr) is slightly lower than the South Tasman value of 51 ± 42 yr on average (ranging from -29 and 176 yr). This indicates weak influences of the EAC on, and contribution of sub-Antarctic waters to, the South Tasman sites during the late LIA as suggested by Komugabe-Dixson et al. (2016), but the contribution of sub-Antarctic waters is small. For the period ~1.8-2.8 cal. kyr BP, both data sets show similar patterns with similar negative anomalies of ~200-250 yr, indicating strong influence of the EAC on the South Tasman sites allowing ^{14}C-enriched waters from the east, due to suppressed ocean upwelling in the TEP and enhanced SEC under El Niño conditions, to reach the Tasman Sea (Komugabe-Dixson et al., 2016).

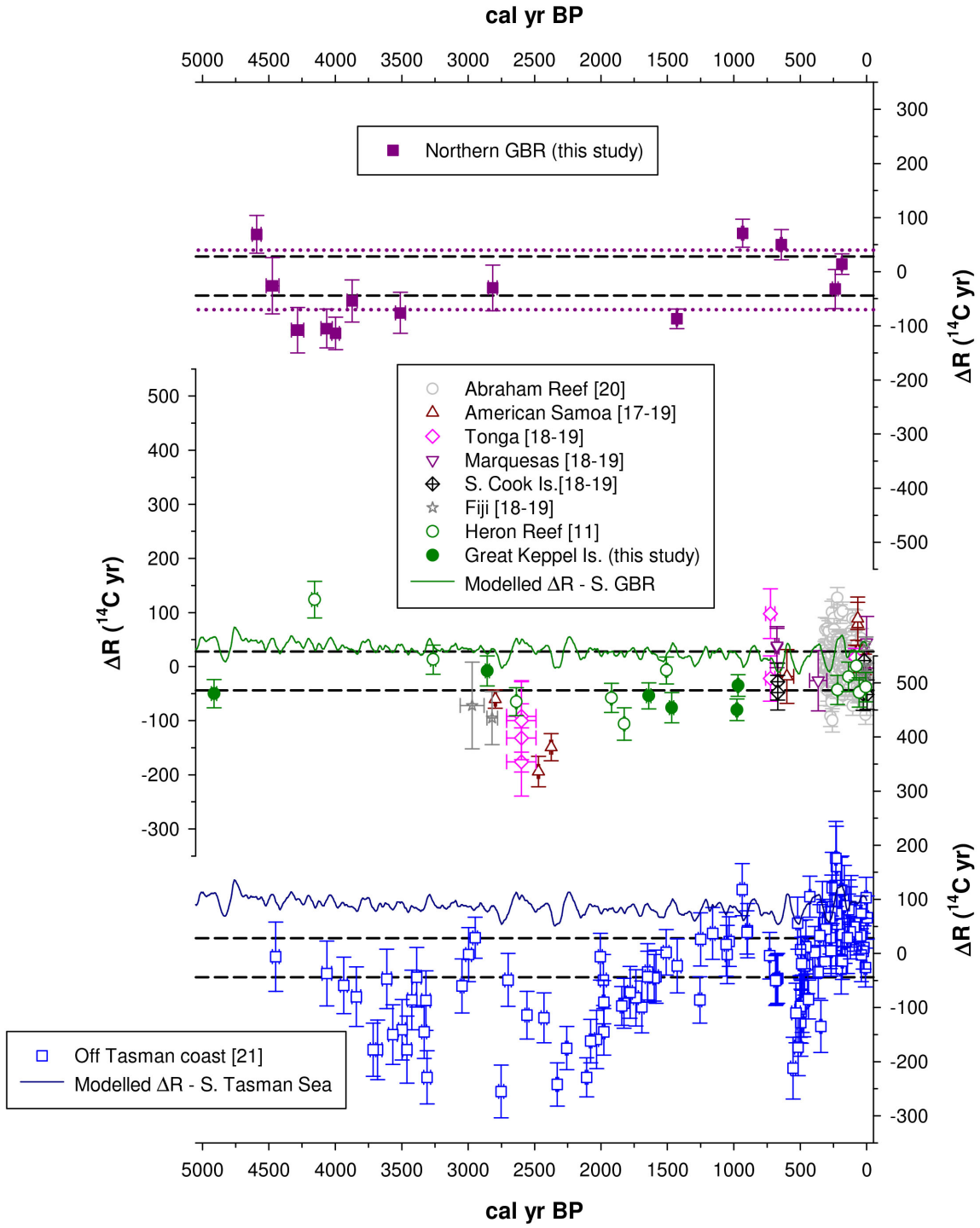

Figure 7. Temporal ΔR variability along the South Pacific Gyre, and in the northern GBR and the South Tasman Sea during the past 5 cal. kyr BP. Sources of published ΔR values are [17] Clark et al. (2016), [18] Petchey et al. (2008), [19] Petchey (2020), [7] Fairbanks et al. (2005), [11] Hua et al. (2015), [20] Druffel and Griffin (1993, 1999) and [21] Komugabe-Dixson et al. (2016). Dashed and dotted lines represent 1σ range of the modern ΔR values for the southern and northern GBR, respectively. Solid lines depict temporal variability in modelled ΔR values for Heron Reef in the southern GBR (middle panel) and the South Tasman Sea (bottom panel) derived from Butzin et al. (2017) and Alves et al. (2019).Vertical error bars are 1σ. Horizontal error bars are 1σ for paired terrestrial/marine samples ([18-19]), and 2σ for corals (all other samples).

Our ΔR values for the northern GBR during the past 5 cal. kyr BP are also plotted to the top panel of Fig. 7 for comparison with those for the South Pacific gyre and South Tasman sites. As there are not many overlapping data between the northern GBR and the South Pacific gyre, no conclusion can be drawn for these two data sets. Although there are several ΔR values for the northern GBR available during ~3-4.5 cal. kyr BP, their variability pattern is similar to that for the South Tasman sites with ΔR (within 1σ range of their modern value) decreasing around 4.5 cal. kyr BP then returning to their modern value at ~3 cal. kyr BP. However, the lowest ΔR value for the northern GBR during this period of ca. -115 yr is much higher than that for the South Tasman sites of ca. -250 yr (see Fig. 7). As the main surface waters in the South Pacific gyre, the northern GBR and South Tasman sites originate from the southern branch of the SEC, similar ΔR variability patterns among these three regions are observed (i.e., the past ~0.3-0.4 and ~1.8-2.8 cal. kyr BP between the gyre and South Tasman sites, and ~3-4.5 cal. kyr BP between the northern GBR and South Tasman sites; see Fig. 7). However, differences in their ΔR values are also evident: the past ~0.3-0.4 cal. kyr BP between the gyre and South Tasman sites, and ~3-4.5 cal. kyr BP between the northern GBR and South Tasman sites (see Fig. 7). This variability is likely caused by differential patterns of water transport, upwelling and mixing between the major currents along the eastern seaboard of Australia (i.e., the GPC, EAC, EAC extension and TF). More ΔR values along the path of the gyre and the northern GBR for the past ~4.5 cal. kyr BP are therefore needed for better understanding of the mechanisms for temporal ΔR variations in these three regions.

Variations in ΔR of ~180-250 yr in magnitude for the southwestern Pacific and along the South Pacific gyre during Late Holocene are not large. Variability in Pacific-wide ocean circulation in transporting surface waters from the TEP to the central and western Pacific is still an important mechanism responsible for such ΔR changes (e.g., negative ΔR anomalies during ~1.8-2.8 cal. kyr BP for the South Pacific gyre and ~1.9-4 cal. kyr BP for the South Tasman) even though variability in the ^{14}C level of the TEP surface waters during this period is not large as seen in the Early to Middle Holocene (Hua et al., 2015).

4.4. Implications for radiocarbon dating

Accurate calendar age determination for marine samples at a particular site/area by taking into account temporal ΔR variability instead of a constant modern ΔR value has been discussed (e.g., Ortlieb et al., 2011; Hua et al., 2015; Petchey, 2020). Butzin et al. (2017) modelled temporal and spatial changes in surface ocean ^{14}C ages using a 3D ocean model, taking into account changes in surface air temperature, wind stress, wind speed, atmospheric CO_2 concentration, freshwater fluxes and atmospheric radiocarbon (i.e., IntCal13; Reimer et al., 2013). We extracted the modelled marine ^{14}C ages for several sites/areas in the Tropical and South Pacific for the Holocene from the model output using the software program developed by Alves et al. (2019), and converted them to modelled ΔR values, which are plotted in Figs. 5-7 for comparison with the observed ΔR data. The modelled ΔR values at each site/area are similar for the Holocene although they are slightly elevated during the Middle Holocene (~50 yr or less), indicating that the modelling does not fully reproduce the larger ΔR variations of several hundred to a thousand years during the Middle Holocene (Fig. 6), and a couple of hundred years observed during the Late Holocene (Fig. 7). As some of the sites/areas shown in Figs. 5-7 are coastal areas from continental margins or marginal seas, which are not properly resolved by the coarse-resolution ocean model, modelling results for these sites/areas might be biased (Butzin et al., 2017). However, even for open ocean sites such as Vanuatu (Fig. 6) and Heron Reef in the southern GBR (middle panel of Fig. 7), the modelling results do not fully reflect temporal changes in

the observed ΔR data. Ocean circulation changes were considered in the model for the period 11.5-50 cal. kyr BP with the employment of three different climatic background conditions. Two of these are glacial scenarios, GS and CS, in which the respective strengths of the meridional overturning circulation (MOC) decrease by ~30% and ~60% compared to the other scenario, the present-day (PD) climatic boundary conditions representing the Holocene and interstadials. However, only the PD scenario was utilised for the past 11.5 cal. kyr BP. In addition, changes in wind stress and wind speed of the model forcing fields during the Holocene may result in ocean circulation variations. Such variations in the model might not well reflect regional and basin-wide ocean circulation changes, in particular, for the Pacific. This is a possible reason for seeing the discrepancies between the observed and modelled ΔR values.

As no modelling work so far has successfully reproduced temporal variability in the observed ΔR data for the Tropical and South Pacific, local/regional ΔR curves based on these empirical data should be constructed for age calibration for improved radiocarbon dating of marine samples. These curves can be constructed using the statistical modelling approach proposed by Toth et al. (2017) or the moving average method employed by Petchey (2020). Alternatively, temporal ΔR variability for each site/area of interest can be taken into account when calibrating marine samples using weighted mean ΔR values for different periods as suggested by Hua et al. (2015). For example, the weighted mean ΔR values for the SCS are 173 ± 95 yr (n = 22) for 5.5-8.1 cal. kyr BP, 109 ± 66 yr (n = 10) for 2-3.5 cal. kyr BP and 2 ± 53 (n=14) for the other time intervals in the past 8.1 cal. kyr BP, including the recent past (Fig. 2a). For the northern GBR, the weighted mean ΔR values are 152 ± 162 yr (n = 7) and -26 ± 63 yr (n=17) for the periods 5.5-7 cal. kyr BP and the past 5.5 cal. kyr BP, respectively (Fig. 2b).

5. Conclusion

We have carried out ^{14}C analyses of ^{230}Th-dated corals collected from the SCS and the GBR for the investigation of temporal variability in the marine radiocarbon reservoir effect at these regions during the Holocene. The results show large ΔR variability of several hundred years during the Middle Holocene for the SCS (~410 yr from trough to peak) and northern GBR (~490 yr), and smaller ΔR changes of ~200 yr during the Late Holocene for the SCS.

Our data, together with previously published ΔR values for the Tropical and South Pacific, indicate the following features of ΔR variations and their possible mechanisms. Firstly, variability in ocean upwelling and changes in the ^{14}C level (or sources) of the upwelled waters are mainly responsible for temporal ΔR variations in coastal areas along the eastern Pacific during the Holocene. Secondly, large ΔR variability of several hundred to a thousand years across the Tropical Pacific during ~5-8 cal. kyr BP reflects variability in ocean circulation associated with climate change in transport of ^{14}C-depleted upwelled waters in the TEP (more contribution of old SAMW and/or AAIW to the upwelled waters and higher/stronger upwelling due to dominant La Niña conditions) and along the equator to the TWP. This might be the main mechanism for the observed ΔR variations across the Pacific, although local/regional effects might also contribute to these changes (e.g., EASM variability for the SCS and changes in local/regional ocean upwelling and/or horizontal advection for the northern GBR). Finally, reduced ΔR variability of a couple of hundred years is evident for the SW Pacific and South Pacific gyre during the Late Holocene. Although variability in the ^{14}C level of the TEP surface waters during this period is not as large as during the Early to Middle Holocene, variability in Pacific-wide ocean circulation in transporting surface waters from the TEP to the west might be still an important

mechanism responsible for ΔR variability for the central and western Pacific during the Late Holocene.

Three-dimensional ocean modelling (Butzin et al., 2017), which takes into account effects of climate change, does not fully reproduce temporal variability in the empirical ΔR values for the Tropical and South Pacific during the Holocene, possibly due to ocean circulation changes for the Holocene were not well represented in the modelling. This indicates the need for construction of local/regional marine radiocarbon calibration curves, which take into account temporal ΔR variability, for accurate age determination of marine samples by radiocarbon dating.

Acknowledgements

This research was supported by the Australian Institute of Nuclear Science and Engineering (project numbers AINGRA08063, AINGRA06181) and ANSTO's Environmental Change Program, and an Australian Research Council Future Fellowship awarded to SU (project number FT120100656). U-Th dating for this study was funded by the National Environmental Research Programme Tropical Ecosystems Hub Project 1.3 to JZ, JMP and TRC, and Australian Research Council Discovery DP180102526 to JZ. AMS radiocarbon analysis at the Centre for Accelerator Science at ANSTO was financially supported by the Australian Government through the National Collaborative Research Infrastructure Strategy. We would like to thank Stuart Hankin for the preparation of Figures 1 and 4. We also thank Karina Meredith for useful discussion on $\delta^{13}C$ of groundwater DIC, and Eduardo Alves for useful advice on the extraction of Butzin et al. (2017)'s modelled CRA time slices using the software developed by Alves et al. (2019). Ian Loch (Australian Museum) assisted with locating and loaning pre-bomb live-collected shellfish.

References

Alves, E., Macario, K., Ascough, P., Bronk Ramsey, C., 2018. The worldwide marine radiocarbon reservoir effect: definitions, mechanisms, and prospects. Rev. Geophys. 56, 1-28, doi:10.1002/2017RG000588.

Alves, E.Q., Macario, K.D., Urrutia, F.P, Cardoso, R.P., Bronk Ramsey, C., 2019. Accounting for the marine reservoir effect in radiocarbon calibration. Quat. Sci. Rev. 209, 129-138, doi:10.1016/j.quascirev.2019.02.013.

Ascough, P.L., Cook, G.T., Dugmore, A.J., 2009. North Atlantic marine ^{14}C reservoir effects: Implications for late-Holocene chronological studies. Quat. Geochronol. 4, 171-180, doi:10.1016/j.quageo.2008.12.002.

van Beek, P., Reyss, J.-L., Paterne, M., Gersonde, R., van der Loeff, M.R., Kuhn, G., 2002. ^{226}Ra in barite: absolute dating of Holocene Southern Ocean sediments and reconstruction of sea-surface reservoir ages. Geology 30, 731-734, doi:10.1130/0091-7613(2002)030<0731:RIBADO>2.0.CO;2.

Bolton, A., Goodkin, N.F., Druffel, E.R.M., Griffin, S., Murty, S.A., 2016. Upwelling of Pacific Intermediate Water in the South China Sea revealed by coral radiocarbon record. Radiocarbon 58, 37-53, doi:10.1017/RDC.2015.4.

Bondevik, S., Mangerud, J., Birks, H.H., Gulliksen, S., Reimer, P., 2006. Changes in North Atlantic radiocarbon reservoir ages during the Allerød and Younger Dryas. Science 312, 1514-1517, doi:10.1126/science.1123300.

Bostock, H.C., Opdyke, B.N., Gagan, M.K., Kiss, A.E., Fifield, L.K., 2006. Glacial/interglacial changes in the East Australian current. Clim. Dyn. 26, 645-659, doi:10.1007/s00382-005-0103-7.

Bryan, E., Meredith, K.T., Baker, A., Andersen, M.S., Post, V.E.A., 2017. Carbon dynamics in a Late Quaternary-age coastal limestone aquifer system undergoing saltwater intrusion. Sci. Total Environ. 607-608, 771-785, doi:10.1016/j.scitotenv.2017.06.094.

Burr, G.S., Haynes, C.V., Shen, C.-C., Taylor, F., Chang, Y.-W., Beck, J.W., Nguyen, V., Zhou, W., 2015. Temporal variations of radiocarbon reservoir ages in the south Pacific ocean during the Holocene. Radiocarbon 57, 507-515, doi:10.1017/S0033822200034871.

Butzin, M., Köhler, P., Lohmann, G., 2017. Marine radiocarbon reservoir age simulations for the past 50,000 years. Geophys. Res. Lett. 44, 8473-8480, doi:10.1002/2017GL074688.

Carpenter, K.E., Niem, V.H. (eds) 1998 FAO Species Identification Guide for Fishery Purposes. The Living Marine Resources of the Western Central Pacific. Volume 1. Seaweeds, Corals, Bivalves and Gastropods. Rome: Food and Agricultural Organisation of the United Nations.

Carré, M., Jackson, D., Maldonado, A., Chase, B.M., Sachs, J.P., 2016. Variability of ^{14}C reservoir age and air–sea flux of CO_2 in the Peru-Chile upwelling region during the past 12,000 years. Quat. Res. 85, 87-93, doi:10.1016/j.yqres.2015.12.002.

Checkley, D.M., Barth, J.A., 2009. Patterns and processes in the California Current System. Prog. Oceanogr. 83, 49-64, doi:10.1016/j.pocean.2009.07.028.

Cheng, H., Edwards, R.L., Hoff, J., Gallup, C.D., Richards, D.A., Asmerom, Y., 2000. The half-lives of uranium-234 and thorium-230. Chem. Geol.169, 17-33, doi:10.1016/S0009-2541(99)00157-6.

Choukroun, S., Ridd, P.V., Brinkman, R., McKinna, L.I.W., 2010. On the surface circulation in the western Coral Sea and residence times in the Great Barrier Reef. J. Geophys. Res. 115, C06013, doi:10.1029/2009JC005761.

Clark, J.T., Quintus, S., Weisler, M., St Pierre, E., Nothdurft, L., Feng, Y., Hua, Q., 2016. Marine reservoir correction for American Samoa using U-series and AMS dated corals. Radiocarbon 58, 851-868, doi:10.1017/RDC.2016.53.

Clark, T.R., Zhao, J.-X., Feng, Y.-X., Done, T.J., Jupiter, S., Lough, J., Pandolfi, J.M., 2012. Spatial variability of initial $^{230}Th/^{232}Th$ in modern Porites from the inshore region of the Great Barrier Reef. Geochim. Cosmochim. Acta 78, 99-118, doi:10.1016/j.gca.2011.11.032.

Clark, T.R., Zhao, J.-x., Roff, G., Feng, Y.-x., Done, T.J., Nothdurft, L.D., Pandolfi, J.M., 2014. Discerning the timing and cause of historical mortality events in modern Porites from the Great Barrier Reef. Geochim. Cosmochim. Acta 138, 57-80, doi:10.1016/j.gca.2014.04.022.

Conroy, J.L., Overpeck, J.T., Cole, J.E., Shanahan, T.M., Steinitz-Kannan, M., 2008. Holocene changes in eastern tropical Pacific climate inferred from a Galápagos lake sediment record. Quat. Sci. Rev. 27, 1166-1180, doi:10.1016/j.quascirev.2008.02.015.

Cutler, K.B., Gray, S.C., Burr, G.S., Edwards, R.L., Taylor, F.W., Cabioch, F., Beck, J.W., Cheng, H., Moore, J., 2004. Radiocarbon calibration and comparison to 50 kyr BP with paired ^{14}C and ^{230}Th dating of corals from Vanuatu and Papua New Guinea. Radiocarbon 46, 1127-1160, doi:10.1017/S0033822200033063.

Dang, P.X., Mitsuguchi, T., Kitagawa, H., Shibata, Y., Kobayashi, T., 2004. Marine reservoir correction in the South of Vietnam estimated from an annually-banded coral. Radiocarbon 46, 657-660, doi:10.1017/S0033822200035712.

Driscoll, R., Elliot, M., Russon, T., Welsh, K., Yokoyama, Y., Tudhope, A., 2014. ENSO reconstructions over the past 60ka using giant clams (*Tridacna* sp.) from Papua New Guinea. Geophys. Res. Lett. 41, doi:10.1002/2014GL061446.

Druffel, E.R.M., 1997. Geochemistry of corals: Proxies of past ocean chemistry, ocean circulation, and climate. Proc. Natl. Acad. Sci. U.S.A. 94, 8354-8361, doi:10.1073/pnas.94.16.8354.

Druffel, E.R.M., Griffin, S., 1993. Large variations of surface ocean radiocarbon: evidence of circulation changes in the southwestern Pacific. J. Geophys. Res.98 (C11), 20249-20259, doi:10.1029/93JC02113.

Druffel, E.R.M., Griffin, S., 1999. Variability of surface ocean radiocarbon and stable isotopes in the southwestern Pacific. J. Geophys. Res.104 (C10), 23607-23613, doi:10.1029/1999JC900212.

Druffel, E.R.M., Griffin, S., Guilderson, T.P., Kashgarian, M., Southon, J., Schrag, D.P., 2001. Changes of subtropical North Pacific radiocarbon and correlation with climate variability. Radiocarbon 43, 15-25, doi:10.1017/S0033822200031593.

Dykoski, C.A., Edwards, R.L., Cheng, H., Yuan, D., Cai, Y., Zhang, M., Lin, Y., Qing, J., An, Z., Revenaugh, J., 2005. A high-resolution, absolute-dated Holocene and deglacial Asian monsoon record from Dongge Cave, China. Earth Planet. Sci. Lett. 233, 71-86, doi:10.1016/j.epsl.2005.01.036.

Edwards, R.L., Beck, J.W., Burr, G.S., Donahue, D.J., Chappell, J.M.A., Bloom, A.L., Druffel, E.R.M., Taylor, F.W., 1993. A large drop in atmospheric $^{14}C/^{12}C$ and reduced melting in the Younger Dryas, documented with ^{230}Th ages of corals. Science 260, 962-968, doi:10.1126/science.260.5110.962.

Fairbanks, R.G., Mortlock, R.A., Chiu, T.-C., Cao, L., Kaplan, A., Guilderson, T.P., Fairbanks, T.W., Bloom, A.L., Grootes, P.M., Nadeau, M.-J., 2005. Radiocarbon calibration curve spanning 0 to 50,000 years BP based on paired $^{230}Th/^{234}U/^{238}U$ and ^{14}C dates on pristine corals. Quat. Sci. Rev. 24, 1781-1796, doi:10.1016/j.quascirev.2005.04.007.

Fan, T., Yu, K., Zhao, J.-x., Jiang, W., Xu, S., Zhang, Y., Wang, R., Wang, Y., Feng, Y., Bian, L., Qian, H., Liao, W., 2020. Strontium isotope stratigraphy and paleomagnetic age constraints on the evolution history of coral reef islands, northern South China Sea. Geological Society of American Bulletin 132(3-4), 803-816, doi:10.1130/B35088.1.

Fass, T., Cook, P.G., Stieglitz, T., Herczeg, A.L., 2007. Development of saline ground water through transpiration of sea water. Groundwater 45, 703-710, doi:10.1111/j.1745-6584.2007.00344.x.

Fink, D., Hotchkis, M., Hua, Q., Jacobsen, G., Smith, A.M., Zoppi, U., Child, D., Mifsud, C., van der Gaast, H., Williams, A., Williams, M., 2004. The ANTARES AMS facility at ANSTO. Nucl. Instrum. Methods B 223-224, 109-115, doi:10.1016/j.nimb.2004.04.025.

Guilderson, T.P., Schrag, D.P., Cane, M.A., 2004. Surface water mixing in the Solomon Sea as documented by a high-resolution coral ^{14}C record. J. Clim. 17, 1147-1157.

Hirabayashia S., Yokoyama, Y., Suzuki, A., Esat, T., Miyairi, Y., Aze, T., Siringan, F., Maeda, Y., 2019. Local marine reservoir age variability at Luzon Strait in the South China Sea during the Holocene. Nucl. Instrum. Methods B 455, 171-177, doi:10.1016/j.nimb.2018.12.001.

Hong, H., Zhang, C., Shang, S., Huang, B., Li, Y., Li, X., Zhang, S., 2009. Interannual variability of summer coastal upwelling in the Taiwan Strait. Cont. Shelf Res. 29, 479-484, doi:10.1016/j.csr.2008.11.007.

Hu, D., Wu, L., Cai, W., Gupta, A.S., Ganachaud, A., Qiu, B., Gordon, A.L., Lin, X., Chen, Z., Hu, S., Wang, G., Wang, Q., Sprintall, J., Qu, T., Kashino, Y., Wang, F., Kessler1, W.S., 2015. Pacific western boundary currents and their roles in climate. Nature 522, 299-308, doi:10.1038/nature14504.

Hu, J., Kawamura, H., Hong, H., Qi, Y., 2000. A review on the currents in the South China Sea: Seasonal circulation, South China Sea Warm Current and Kuroshio intrusion. J. Oceanogr. 56, 607-624.

Hua, Q., 2015. Radiocarbon dating of marine carbonates. In: Rink, W.J., and Thompson, J. (Eds.), Encyclopedia of Scientific Dating Methods. Earth Sciences Series, Springer, Netherlands, p.676-679, doi:10.1007/978-94-007-6326-5_151-1.

Hua, Q., Jacobsen, G.E., Zoppi, U., Lawson, E.M., Williams, A.A., Smith, A.M., McGann, M.J., 2001. Progress in radiocarbon target preparation at the ANTARES AMS Centre. Radiocarbon 43, 275-282, doi:10.1017/S003382220003811X.

Hua, Q., Woodroffe, C.D., Barbetti, M., Smithers, S.G., Zoppi, U., Fink, D., 2004. Marine reservoir corrections for the Cocos (Keeling) Islands, Indian Ocean. Radiocarbon 46, 603-610, doi:10.1017/S0033822200035645.

Hua, Q., Barbetti, M., Fink, D., Kaiser, K.F., Friedrich, M., Kromer, B., Levchenko, V.A., Zoppi, U., Smith, A.M., Bertuch, F., 2009. Atmospheric ^{14}C variations derived from tree rings during the early Younger Dryas. Quat. Sci. Rev. 28, 2982-2990, doi:10.1016/j.quascirev.2009.08.013.

Hua, Q., Webb, G.E., Zhao, J.-x., Nothdurft, L.D., Lybolt, M., Price, G.J., Opdyke, B.N., 2015. Large variations in the Holocene marine radiocarbon reservoir effect reflect ocean circulation and climatic changes. Earth Planet. Sci. Lett. 422, 33-44, doi:10.1016/j.epsl.2015.03.049.

Jell, P.A., 2013. Geology of Queensland. Geological Survey of Queensland, Brisbane.

Komugabe-Dixson, A.F., Fallon, S.J., Eggins, S.M., Thresher, R.E., 2016. Radiocarbon evidence for mid-late Holocene changes in southwest Pacific Ocean circulation. Paleoceanography 31, 971-985, doi: 10.1002/2016PA002929.

Kessler, W.S., Cravatte, S., 2013. Mean circulation of the Coral Sea. J. Geophys. Res. 118, 6385-6410, doi:10.1002/2013JC009117.

Latorre, C., De Pol-Holz, R., Carter, C., Santoro, C.M., 2017. Using archaeological shell middens as a proxy for past local coastal upwelling in northern Chile. Quat. Int. 427, 128-136, doi:10.1016/j.quaint.2015.11.079.

Leonard, N.D., Zhao, J.-x., Welsh, K.J., Feng, Y.-x., Smithers, S.G., Pandolfi, J.M., Clark, T.R., 2016. Holocene sea level instability in the southern Great Barrier Reef, Australia: high-precision U-Th dating of fossil microatolls. Coral Reefs 35, 625-639, doi:10.1007/s00338-015-1384-x.

Leonard, N.D., Welsh, K.J., Clark, T.R., Feng, Y.x., Pandolfi, J.M., Zhao, J.x., 2018. New evidence for "far-field" Holocene sea level oscillations and links to global climate records. Earth Planet. Sci. Lett. 487, 67-73, doi:10.1016/j.epsl.2018.02.008.

Lewis, S.E., Wüst, R.A.J., Webster, J.M., Shields, G.A., Renema, W., Lough, J.M., Jacobsen, G., 2012. Development of an inshore fringing coral reef using textural, compositional and stratigraphic data from Magnetic Island, Great Barrier Reef, Australia. Mar. Geol. 299-302, 18-32, doi:10.1016/j.margeo.2012.01.003.

Lewis, S.E., Sloss, C.R., Murray-Wallace, C.V., Woodroffe, C.D., Smithers, S.G., 2013. Post-glacial sea-level changes around the Australian margin: a review. Quat. Sci. Rev. 74, 115-138, doi:10.1016/j.quascirev.2012.09.006.

Lindauer, S., Santos, G.M., Steinhof, A., Yousif, E., Phillips, C., Jasim, S.A., Uerpmann, H.-P., Hinderer, M., 2017. The local marine reservoir effect at Kalba (UAE) between the Neolithic and Bronze Age: An indicator of sea level and climate changes. Quat. Geochronol. 42, 105-116, doi:10.1016/j.quageo.2017.09.003.

Liu, Q., Kaneko, A., Jilan, S., 2008. Recent progress in studies of the South China Sea circulation. J. Oceanogr. 64, 753-762.

Liu, Z., Lu, Z., Wen, X., Otto-Bliesner, B.L., Timmermann, A., Cobb, K.M., 2014. Evolution and forcing mechanisms of El Niño over the past 21,000 years. Nature 515, 550-553, doi:10.1038/nature13963.

Ludwig, K.R., 2003. Users manual for Isoplot/Ex version 3.0: a geochronological toolkit for Microsoft Excel. Berkeley Geochronol. Centre Spec. Pub., vol.3. Berkeley.

McGregor, H.V., Gagan, M.K., McCulloch, M.T., Hodge, E., Mortimer, G., 2008. Mid-Holocene variability in the marine ^{14}C reservoir age for northern coastal Papua New Guinea. Quat. Geochronol. 3, 213-225, doi:10.1016/j.quageo.2007.11.002.

McGregor, H.V., Fischer, M.J., Gagan, M.K., Fink, D., Phipps, S.J., Wong, H., Woodroffe, C.D., 2013. A weak El Niño/Southern Oscillation with delayed seasonal growth around 4300 years ago. Nat. Geosci. 6, 949-953, doi:10.1038/NGEO1936.

Meredith, K.T., Han, L.F., Cendón, D.I., Crawford, J., Hankin, S., Peterson, M., Hollins, S.E., 2018. Evolution of dissolved inorganic carbon in groundwater recharged by cyclones and groundwater age estimations using the ^{14}C statistical approach. Geochim. Cosmochim. Acta 220, 483-498, doi:10.1016/j.gca.2017.09.011.

Merino-Campos, V., De Pol-Holz, R., Southon, J., Latorre, C., Collado-Fabbri, S., 2019. Marine radiocarbon reservoir age along the Chilean continental margin. Radiocarbon 61, 195-210, doi:10.1017/RDC.2018.81.

Middleton, J.F., Cirano, M., 2005. Wintertime circulation off southeast Australia: Strong forcing by the East Australian Current. J. Geophys. Res. 110, C12012, doi:10.1029/2004JC002855.

Moore, W.S., 2010. The effect of submarine groundwater discharge on the ocean. Annu. Rev. Mar. Sci. 2, 59-88, doi: 10.1146/annurev-marine-120308-081019.

Morimoto, M., Kitagawa, H., Shibata, Y., Kayanne, H., 2004. Seasonal radiocarbon variation of surface seawater recorded in a coral from Kikai Island, subtropical northwestern Pacific. Radiocarbon 46, 643-648, doi:10.1017/S0033822200035694.

Moy, C.M., Seltzer, G.O., Rodbell, D.T., Anderson, D.M., 2002. Variability of El Niño/Southern Oscillation activity at millennial timescales during the Holocene epoch. Nature 420, 162-165, doi:10.1038/nature01194.

Nan, F., Xue, H., Yu, F., 2019. Kuroshio intrusion into the South China Sea: A review. Prog. Oceanogr. 137, 314-333, doi:10.1016/j.pocean.2014.05.012.

Nothdurft, L., Webb, G., 2009. Earliest diagenesis in scleractinian coral skeletons: implications for palaeoclimate-sensitive geochemical archives. Facies 55, 161-201, doi:10.1007/s10347-008-0167-z.

O'Connor, S., Ulm, S., Fallon, S.J., Barham. A., Loch, I., 2010. Pre-bomb marine reservoir variability in the Kimberley region, Western Australia. Radiocarbon 52, 1158-1165, doi:10.1017/S0033822200046233.

Ortlieb, L., Vargas, G., Saliège, J.-F., 2011. Marine radiocarbon reservoir effect along the northern Chile-southern Peru coast (14-24ºS) throughout the Holocene. Quat. Res. 75, 91-103, doi:10.1016/j.yqres.2010.07.018.

Paterne, M., Ayliffe, L.K., Arnold, M., Cabioch, G., Tisnerat-Laborde, N., Hatté, C., Douville, E., Bard, E., 2004. Paired ^{14}C and $^{230}Th/U$ dating of surface corals from the Marquesas and Vanuatu (sub-equatorial Pacific) in the 3000 to 15,000 cal yr interval. Radiocarbon 46, 551-566, doi:10.1017/S0033822200035608.

Petchey, F., 2009. Dating marine shell in Oceania: issues and prospects. In Fairbairn, A., O'Connor, S., and Marwick, B. (eds.), Terra Australis 28: New Directions in Archaeological Science. Canberra: ANU E Press, pp. 157-172.

Petchey, F., 2020. New evidence for a mid- to late-Holocene change in the marine reservoir effect across the South Pacific gyre. Radiocarbon 62, 127-139, doi:10.1017/RDC.2019.103.

Petchey, F., Ulm, S., 2012. Marine reservoir variation in the Bismarck region: an evaluation of spatial and temporal change in ΔR and R over the last 3000 years. Radiocarbon 54, 45-58, doi:10.2458/azu_js_rc.v54i1.13050.

Petchey, F., Anderson, A., Zondervan, A., Ulm, S., Hogg, A., 2008. New marine ΔR values for the South Pacific Subtropical Gyre region. Radiocarbon 50, 373-397, doi:10.1017/S0033822200053509.

Qiu, B., 2001. Kuroshio and Oyashio Currents. In Encyclopedia of Ocean Sciences (2nd Edn), edited by John H. Steele, Academic Press, 2001, pp. 358-369.

Reeves, J.M., Bostock, H.C., Ayliffe, L.K., Barrows, T.T., De Deckker, P., Devriendt, L.S., Dunbar, G.B., Drysdale, R.N., Fitzsimmons, K.E., Gagan, M.K., Griffiths, M.L., Haberle, S.G., Jansen, J.D., Krause, C., Lewis, S., McGregor, H.V., Mooney, S.D., Moss, P., Nanson, G.C., Purcell, A., van der Kaars, S., 2013. Palaeoenvironmental change in tropical Australasia over the last 30,000 years – a synthesis by the OZ-INTIMATE group. Quat. Sci. Rev. 74, 97-114, doi:10.1016/j.quascirev.2013.01.001.

Reimer, R.W., Reimer, P.J., 2017. An online application for ΔR calculation. Radiocarbon 59, 1623-1627, doi:10.1017/RDC.2016.117.

Reimer, P.J., Baillie, M.G.L., Bard, E., Bayliss, A., Beck, J.W., Blackwell, P.G., Bronk Ramsey, C., Buck, C.E., Burr, G.S., Edwards, R.L., Friedrich, M., Grootes, P.M., Guilderson, T.P., Hajdas, I., Heaton, T., Hogg, A.G., Hughen, K.A., Kaiser, K.F., Kromer, B., McCormac, F.G., Manning, S.W., Reimer, R.W., Richards, D.A., Southon, J.R., Talamo, S., Turney, C.S.M., van der Plicht, J., Weyhenmeyer, C.E., 2009. IntCal09 and Marine09 radiocarbon age calibration curves, 0-50,000 years cal BP. Radiocarbon 51, 1111-1150, doi:10.1017/S0033822200034202.

Reimer, P.J., Bard, E., Bayliss, A., Beck, J.W., Blackwell, P.G., Bronk Ramsey, C., Buck, C., Cheng, H., Edwards, R.L., Friedrich, M., Grootes, P.M., Guilderson, T.P., Haflidason, H., Hajdas, I., Hatteé, C., Heaton, T.J., Hoffmann, D.L., Hogg, A.G., Hughen, K.A., Kaiser, K.F., Kromer, B., Manning, S.W., Niu, M., Reimer, R.W., Richards, D.A., Scott, E.M., Southon, J.R., Staff, R.A., Turney, C.S.M., van der Plicht, J., 2013. IntCal13 and Marine13 radiocarbon age calibration curves 0-50,000 years cal BP. Radiocarbon 55, 1869-1887, doi:10.2458/azu_js_rc.55.16947.

Ridgway, K.R. Dunn, J.R., 2003. Mesoscale structure of the mean East Australian Current System and its relationship with topography. Prog. Oceanogr. 56, 189-222, doi:10.1016/S0079-6611(03)00004-1.

Ridgway, K.R., Benthuysen, J.A., Steinberg, C., 2018. Closing the gap between the Coral Sea and the Equator: Direct observations of the north Australian western boundary currents. J. Geophys. Res. 123, 9212-9231, doi:10.1029/2018JC014269.

Sarnthein, M., Balmer, S., Grootes, P.M., Mudelsee, M., 2015. Planktic and benthic ^{14}C reservoir ages for three ocean basins, calibrated by a suite of ^{14}C plateaus in the Glacial-to-Deglacial Suigetsu atmospheric ^{14}C record. Radiocarbon 57, 129-151, doi:10.2458/azu_rc.57.17916.

Siani, G., Paterne, M., Michel, E., Sulpizio, R., Sbrana, A., Arnold, M., Haddad, G., 2001. Mediterranean sea surface radiocarbon reservoir age changes since the Last Glacial Maximum. Science 294, 1917-1920, doi:10.1126/science.1063649.

Sikes, E.L., Samson, C.R., Guilderson, T.P., Howard, W.R., 2000. Old radiocarbon ages in the southwest Pacific Ocean during the last glacial period and deglaciation. Nature 405, 555-559, doi:10.1038/35014581.

Skinner, L., McCave, I.N., Carter, I., Fallon, S., Scrivner, A.E., Primeau, F., 2015. Reduced ventilation and enhanced magnitude of the deep Pacific carbon pool during the last glacial period. Earth Planet. Sci. Lett. 411, 45-52, doi:10.1016/j.epsl.2014.11.024.

Southon, J., Kashgarian, M., Fontugne, M., Metivier, B., Yim, W.W.S., 2002. Marine reservoir corrections for the Indian Ocean and Southeast Asia. Radiocarbon 44, 167-180, doi:10.1017/S0033822200064778.

Stuiver, M., Polach, H.A., 1977. Discussion: reporting of ^{14}C data. Radiocarbon 19, 355-363, doi:10.1017/S0033822200003672.

Stuiver, M., Pearson, G.W., Braziunas, T., 1986. Radiocarbon age calibration of marine samples back to 9000 cal yr BP. Radiocarbon 28, 980-1021, doi:10.1017/S0033822200060264.

Talley, L.D., Pickard, G.L., Emery, W.J., Swift, J.H., 2011. Descriptive physical oceanography: An introduction. 6th Edition, Academic Press, London.

Tilburg, C.E., Hurlburt, H.E., O'Brien, J.J., Shriver, J.F., 2001. The Dynamics of the East Australian Current System: The Tasman Front, the East Auckland Current, and the East Cape Current. J. Phys. Oceanogr. 31, 2917-2943.

Tomczak, M., Godfrey, J.S., 2001. Regional Oceanography: An Introduction. Version 1.0. Oxford: Elsevier Science Ltd. URL: http://www.es.flinders.edu.au/~mattom/regoc/pdfversion.html.

Toth, L.T., Aronson, R.B., Cheng, H., Edwards, R.L., 2015. Holocene variability in the intensity of wind-gap upwelling in the tropical eastern Pacific. Paleoceanography 30, 1113-1131, doi:10.1002/2015PA002794.

Toth, L.T., Cheng, H., Edwards, R.L., Ashe, E., Richey, J.N., 2017. Millennial-scale variability in the local radiocarbon reservoir age of south Florida during the Holocene. Quat. Geochronol. 42, 130-143, doi:10.1016/j.quageo.2017.07.005.

Turner, S., Bean, L.B., Dettmann, M., McKellar, J.L., McLoughlin, S., Thulborn, T., 2009. Australian Jurassic sedimentary and fossil successions: current work and future prospects for marine and non-marine correlation. Geologiska Föreningens Förhandlingar (GFF) 131, 49-70, doi:10.1080/11035890902924877.

Ulm, S., 2002. Marine and estuarine reservoir effects in central Queensland, Australia: Determination of ΔR values. Geoarchaeology 17(4), 319-348, doi:10.1002/gea.10017.

Ulm, S., Petchey, F., Ross, A., 2009. Marine reservoir corrections for Moreton Bay, Australia. Archaeol. Ocean. 44, 160-166, doi:10.1002/j.1834-4453.2009.tb00060.x.

Wang, Y.J., Cheng, H., Edwards, R.L., He, Y., Kong, X., An, Z., Wu, J., Kelly, M.J., Dykoski, C.A., Li, X., 2005. The Holocene Asian monsoon: Links to solar changes and North Atlantic climate. Science 308, 854-857, doi:10.1126/science.1106296.

Waterhouse, J., Brodie, J., Coppo, C., Tracey, D., 2016. Assessment of the relative risk of degraded water quality to ecosystems of the Cape York NRM Region, Great Barrier Reef. Report to the Department of the Environment and Heritage Protection, Queensland Government, Brisbane - Report 13/28.

Yancheva, G., Nowaczyk, N.R., Mingram, J., Dulski, P., Schettler, G., Negendank, J.F.W., Liu, J., Sigman, D.M., Peterson, L.C., Haug, G.H., 2007. Influence of the intertropical convergence zone on the East Asian monsoon. Nature 445, 74-77, doi:10.1038/nature05431.

Yu, K., Zhao, J.-x., 2009. Coral reefs (of the South China Sea). In: Wang, P.X. and Li, Q.Y. (Eds.), The South China Sea – Paleoceanography and sedimentology. Springer, Dordrecht, The Netherlands, 186-209.

Yu, K.-F., Zhao, J.-X., Liu, T.S., Wei, G.H., Wang, P.X., Collerson, K.D., 2004. High frequency winter cooling and reef coral mortality during the Holocene climatic optimum. Earth Planet. Sci. Lett. 224, 143-155, doi:10.1016/j.epsl.2004.04.036.

Yu, K.-F., Zhao, J.-X., Wei, G.-J., Cheng, X.-R., Wang, P.-X., 2005. Mid-late Holocene monsoon climate retrieved from seasonal Sr/Ca and $\delta^{18}O$ records of *Porites lutea* corals at Leizhou Peninsula, northern coast of South China Sea. Global Planet. Change 47, 301-316, doi:10.1016/j.gloplacha.2004.10.018.

Yu, K., Hua, Q., Zhao, J.-x., Hodge, E., Fink, D., Barbetti, M., 2010. Holocene marine ^{14}C reservoir age variability: evidence from ^{230}Th-dated corals from South China Sea. Paleoceanography 25, PA3205, doi:10.1029/2009PA001831.

Zhang, Y., Yu, K., Qian, H., Fan, T., Yue, Y., Wang, R., Jiang, W., Xu, S., Wang, Y., 2020. The basement and volcanic activities of the Xisha Islands: Evidence from the kilometre-scale drilling in the northwestern South China Sea. Geological Journal 55, 571-583, doi:10.1002/gj.3416.

Zhao, J.X., Xia, Q.K., Collerson, K.D., 2001. Timing and duration of the last inter-glacial inferred from high resolution U-series chronology of stalagmite growth in Southern Hemisphere. Earth Planet. Sci. Lett.184, 635-644, doi:10.1016/S0012-821X(00)00353-8.

Zhao, J., Yu, K., Feng, Y., 2009. High-precision ^{238}U–^{234}U–^{230}Th disequilibrium dating of the recent past: a review. Quat. Geochronol. 4, 423-433, doi:10.1016/j.quageo.2009.01.012.

Zhou, H.Y., Zhao, J.X., Wang, Q., Feng, Y.X., Tang, J., 2011. Speleothem-derived Asian summer monsoon variations in Central China during 54-46 ka. J. Quat. Sci. 26, 781-790, doi:10.1002/jqs.1506.

Supplementary Materials for

Temporal variability in the Holocene marine radiocarbon reservoir effect for the Tropical and South Pacific

Hua, Q., Ulm, S., Yu, K., Clark, T.R., Nothdurft, L.D., Leonard, N.L., Pandolfi, J.M., Jacobsen, G.E., Zhao, J.

This pdf file includes:

Tables S1-S3

Figures S1-S3

References

Supplementary Table S1 - Modern ΔR values for the northern GBR

	Museum #	Shell species	Diet[a]	Location	Collection year	Lab ID	^{14}C Age (BP)		ΔR (^{14}C yr)[b]	
							mean	1σ	mean	1σ
1	C.29757/1	*Arca ventricosa*	SF	Murray Island	1907	OZJ245	445	45	-4	46
2	C.29840/1	*Atactodea striata*	SF	Murray Island	1907	OZJ247	480	30	30	30
3	C.29840/1	*Atactodea striata*	SF	Murray Island	1907	OZL273	380	30	-70	30
Note:						weighted mean ΔR =			-17	56

[a] - SF: suspension feeding

[b] - ΔR and associated uncertainty calculated using the online *deltar* software (Reimer and Reimer, 2017) and the Marine13 data (Reimer et al., 2013)

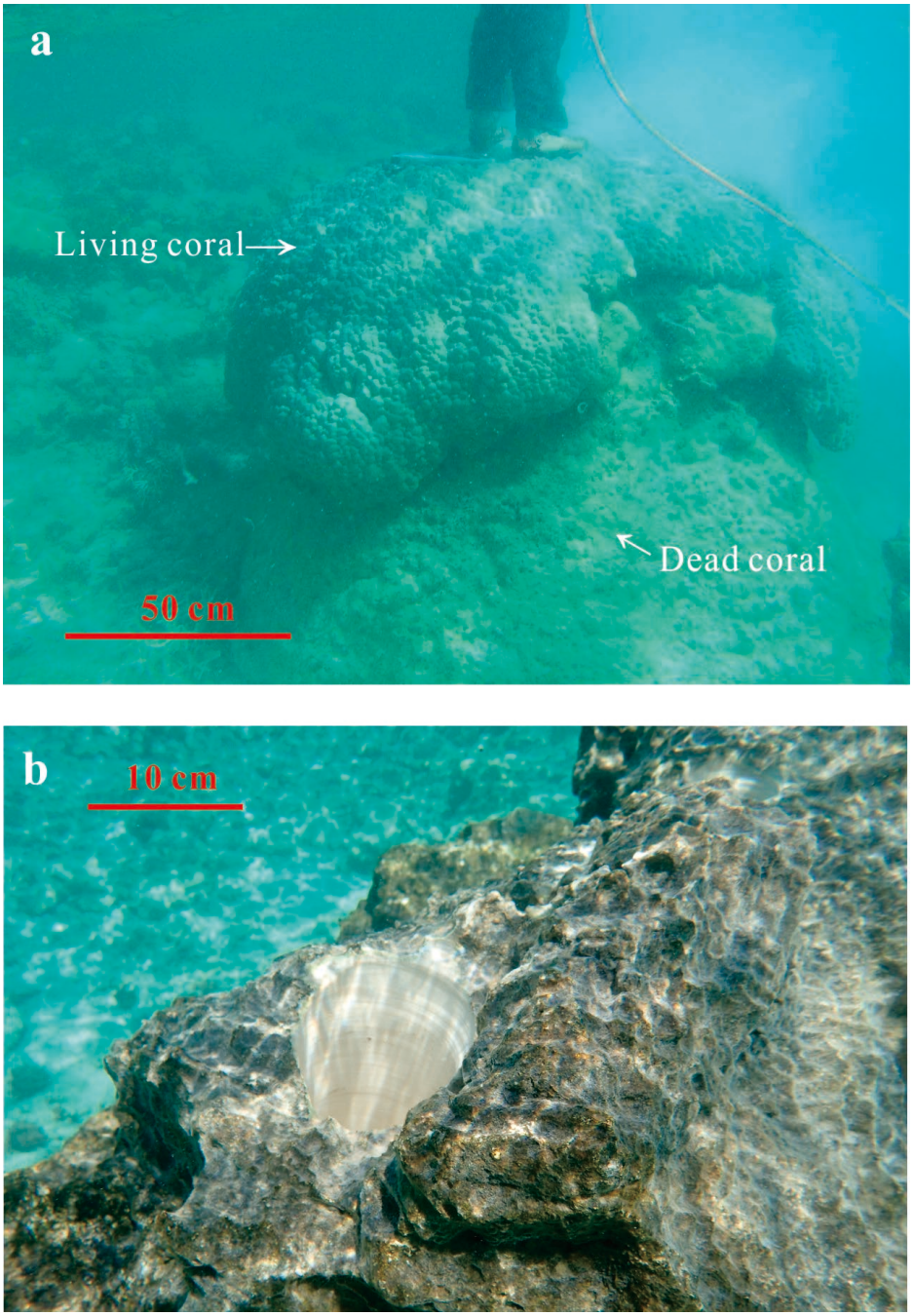

Supplementary Fig. S1 – Field photographs for the study sites in the South China Sea: **(a)** Dead and living corals at the Nansha Islands, and **(b)** Dead corals at the Xisha Islands.

Supplementary Fig. S2 – Field photographs for the study sites in the northern Great Barrier Reef. **(a)** Fossil microatoll from Alexandra Reef, **(b)** Coral core extraction at Gore Island, **(c)** Fossil microatoll from Gore Island, **(d)** Living and fossil corals at Haggerstone Island, and **(e)** Fossil microatoll from Haggerstone Island.

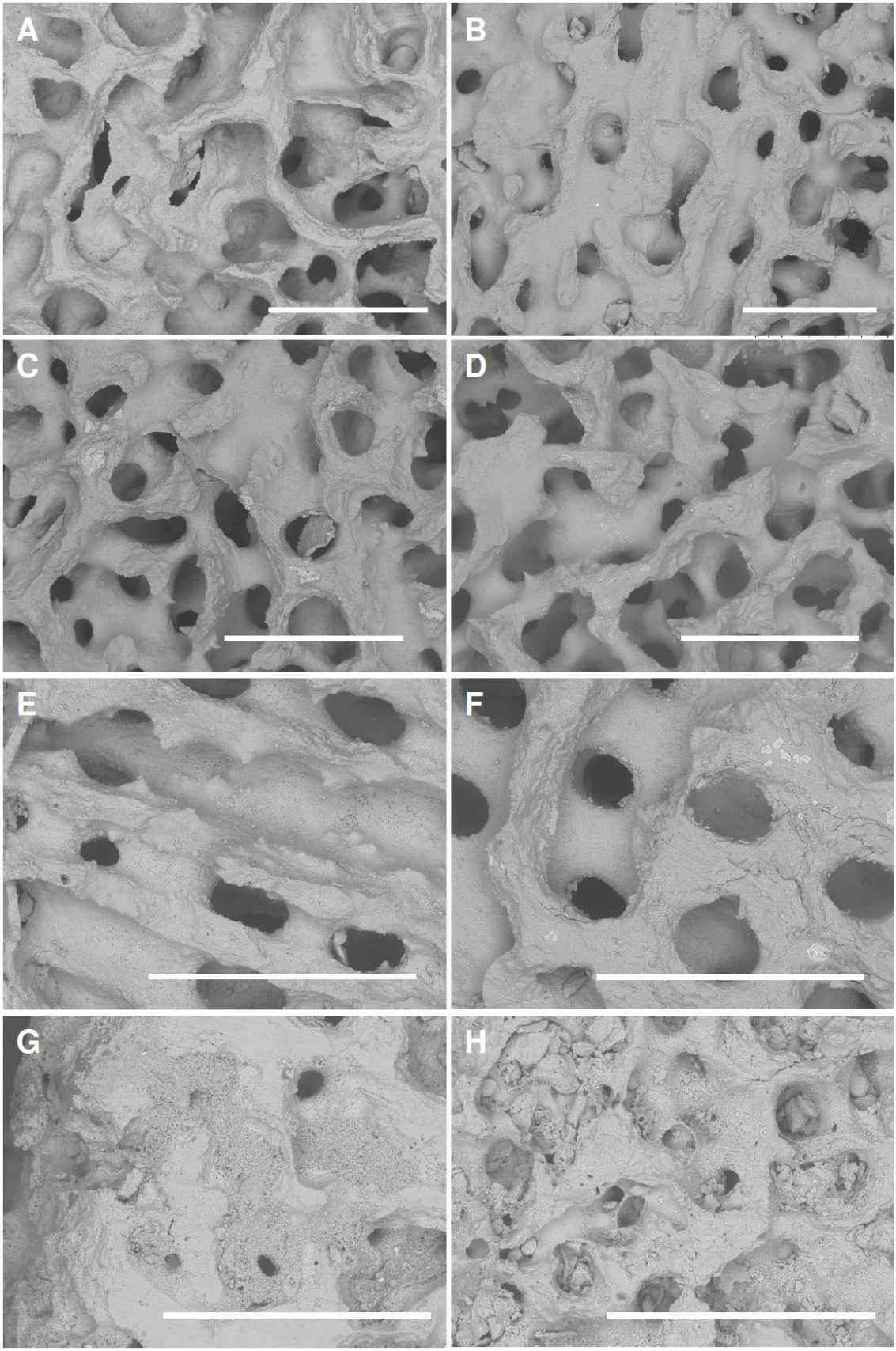

Supplementary Fig. S3 – SEM images of saw cut coral samples. (**A-F**) Clean coral skeletons. Samples reference to Supplementary Table S3. (**A**) *Porites* sp. (GOR N019, OZU734) from Gore Is. (**B**) Unidentified coral (CLE S2RFC1, OZU732) from Clerke Is. (**C**) *Porites* sp. (HIG MA015E2, OZU745) from High Is. (**D**) *Porites* sp. (NK1 009, OZV819) from Great Keppel Is. (**E**) *Porites* sp. (YXD-4, OZM057) from Xisha Is. (**F**) *Porites* sp. (YXO-1, OZM065) from Xisha Is. (**G-H**) Examples of common diagenetic cements in cavities of Holocene coral skeletons that were excluded from this study. (**G**) *Porites* sp. (HAG 10) from Haggerstone Is. (**H**) *Faviid* sp. (GOR S2C3) from Gore Is. Scale bars are 500µm.

Supplementary Table S2 - U Th dating results of corals from the SCS and GBR

	Sample ID	U (ppm)		^{232}Th (ppb)		(^{230}Th/ ^{232}Th)		(^{230}Th/^{238}U)		(^{234}U/ ^{238}U)		Uncorr. ^{230}Th Age (ka)		Corr. ^{230}Th Age (ka)[a]		Corr. ^{230}Th Age (cal BP)[b]		Initial ^{234}U/ ^{238}U		δ^{234}U (T)		Analysis method/Year of measurement
		mean	2σ	mean	2σ	mean	2σ	mean	2σ	mean	2σ	mean	2σ	mean	2σ	mean	2σ	mean	2σ	mean	2σ	
	(1)	(2)	(3)	(4)	(5)	(6)	(7)	(8)	(9)	(10)	(11)	(12)	(13)	(14)	(15)	(16)	(17)	(18)	(19)	(20)	(21)	(22)
Northern GBR - Clerke Island																						
1	CLE S2RFC1	2.9968	0.0023	25.081	0.025	24.05	0.06	0.06633	0.00017	1.1452	0.0011	6.499	0.018	6.334	0.037	6268	37	1.1480	0.0011	148.0	1.1	MC-ICP-MS/2014
	CLE S2RFC1 rep	2.8588	0.0027	19.990	0.039	28.99	0.10	0.06681	0.00021	1.1449	0.0018	6.548	0.023	6.368	0.093	6301	93	1.1478	0.0018	147.8	1.8	MC-ICP-MS/2017
	CLE S2RFC1 mean															6273	35					
2	CLE S1C2	2.5400	0.0013	1.548	0.002	14.06	0.15	0.00282	0.00003	1.1480	0.0009	0.269	0.003	0.251	0.005	187	5	1.1482	0.0009	148.2	1.0	MC-ICP-MS/2014
Northern GBR - Gore Island																						
3	GOR N021	3.1270	0.0015	3.527	0.001	195.12	1.33	0.07253	0.00047	1.1447	0.0011	7.129	0.048	7.103	0.048	7038	48	1.1476	0.0011	147.6	1.1	MC-ICP-MS/2014[c]
4	GOR S2RFC4	2.5911	0.0009	29.332	0.038	19.88	0.07	0.07417	0.00025	1.1422	0.0013	7.311	0.027	7.089	0.052	7023	52	1.1454	0.0013	145.4	1.3	MC-ICP-MS/2014
	GOR S2RFC4 rep	2.5840	0.0031	37.128	0.063	15.58	0.06	0.07379	0.00029	1.1442	0.0014	7.260	0.031	6.888	0.187	6821	187	1.1476	0.0015	147.6	1.5	MC-ICP-MS/2017
	GOR S2RFC4 mean															7009	52					
5	GOR N019	2.8329	0.0013	6.882	0.009	75.00	0.50	0.06005	0.00041	1.1440	0.0008	5.873	0.042	5.822	0.043	5757	43	1.1465	0.0009	146.5	0.9	MC-ICP-MS/2014[c]
	GOR N019 rep	2.7889	0.0029	7.630	0.013	65.52	0.30	0.05908	0.00026	1.1463	0.0014	5.764	0.027	5.693	0.044	5626	44	1.1487	0.0014	148.7	1.4	MC-ICP-MS/2017
	GOR N019 mean															5694	65					
6	GOR N010	2.6430	0.0011	17.678	0.017	26.80	0.20	0.05906	0.00035	1.1432	0.0011	5.778	0.035	5.645	0.044	5580	44	1.1457	0.0011	145.7	1.1	MC-ICP-MS/2014[c]
7	GOR 005	2.4778	0.0016	6.176	0.013	55.20	0.60	0.04532	0.00046	1.1440	0.0009	4.403	0.046	4.349	0.047	4284	47	1.1463	0.0009	146.3	0.9	MC-ICP-MS/2014[c]
8	GOR N006	2.5218	0.0011	19.994	0.026	16.90	0.10	0.04411	0.00029	1.1433	0.0008	4.287	0.028	4.129	0.042	4065	42	1.1452	0.0008	145.2	0.8	MC-ICP-MS/2014[c]
9	GOR N004	2.5509	0.0012	7.858	0.011	37.00	0.40	0.03760	0.00035	1.1449	0.0010	3.639	0.034	3.575	0.037	3510	37	1.1465	0.0010	146.5	1.0	MC-ICP-MS/2014[c]
10	GOR N002	2.8823	0.0016	13.787	0.018	19.60	0.20	0.03086	0.00027	1.1457	0.0006	2.976	0.026	2.880	0.033	2815	33	1.1470	0.0007	147.0	0.7	MC-ICP-MS/2014[c]
11	GOR S1C4	3.6199	0.0018	1.229	0.009	140.04	1.13	0.01567	0.00006	1.1446	0.0010	1.503	0.006	1.492	0.006	1428	6	1.1452	0.0011	145.2	1.1	MC-ICP-MS/2014
12	GOR S3C2	3.0667	0.0014	15.467	0.018	2.54	0.02	0.00422	0.00004	1.1456	0.0010	0.403	0.004	0.302	0.021	237	21	1.1458	0.0010	145.8	1.0	MC-ICP-MS/2014
Northern GBR - Haggerstone Island																						
13	HAG 016	2.6977	0.0015	2.239	0.007	194.30	1.40	0.05315	0.00036	1.1441	0.0008	5.182	0.036	5.161	0.036	5096	36	1.1462	0.0008	146.2	0.8	MC-ICP-MS/2014
14	HAG 002	2.6509	0.0012	6.334	0.010	61.41	0.41	0.04836	0.00031	1.1434	0.0008	4.708	0.031	4.657	0.033	4592	33	1.1454	0.0008	145.4	0.8	MC-ICP-MS/2014[c]
15	HAG 003	2.5732	0.0012	0.468	0.004	699.50	7.40	0.04196	0.00028	1.1436	0.0010	4.073	0.028	4.064	0.028	3999	28	1.1453	0.0010	145.3	1.0	MC-ICP-MS/2014[c]
16	HAG 006	2.4817	0.0010	3.058	0.007	100.79	0.97	0.04093	0.00038	1.1446	0.0011	3.968	0.038	3.939	0.038	3874	38	1.1463	0.0011	146.3	1.1	MC-ICP-MS/2014[c]
17	HAG S2RFC1	3.7297	0.0022	0.442	0.001	269.23	2.04	0.01052	0.00008	1.1467	0.0016	1.005	0.008	0.999	0.008	934	8	1.1472	0.0017	147.2	1.7	MC-ICP-MS/2014
18	HAG S3C2	2.8322	0.0010	3.209	0.004	20.57	0.12	0.00768	0.00004	1.1440	0.0009	0.735	0.004	0.708	0.007	643	7	1.1443	0.0009	144.3	0.9	MC-ICP-MS/2014
Northern GBR - Alexandra Reef																						
19	ALR 043	2.8237	0.0014	9.463	0.013	43.00	0.20	0.04749	0.00020	1.1448	0.0014	4.622	0.021	4.536	0.048	4473	48	1.1468	0.0015	146.8	1.5	MC-ICP-MS/2013[c]
Northern GBR - High Island																						
20	HIG 005C	3.0075	0.0023	13.857	0.030	46.60	0.20	0.07069	0.00017	1.1476	0.0009	6.943	0.018	6.824	0.062	6761	62	1.1491	0.0009	149.1	0.9	MC-ICP-MS/2013[c]
21	HIG MA015E2	2.8629	0.0011	9.775	0.015	60.80	0.10	0.06837	0.00016	1.1433	0.0008	6.724	0.017	6.655	0.039	6592	39	1.1461	0.0008	146.1	0.8	MC-ICP-MS/2013[c]
	HIG MA015E2 rep	2.9663	0.0036	1.652	0.002	372.97	0.97	0.06845	0.00017	1.1477	0.0015	6.698	0.020	6.683	0.021	6616	21	1.1505	0.0015	150.5	1.5	MC-ICP-MS/2017
	HIG MA015E2 mean															6611	18					

	(1)	(2)	(3)	(4)	(5)	(6)	(7)	(8)	(9)	(10)	(11)	(12)	(13)	(14)	(15)	(16)	(17)	(18)	(19)	(20)	(21)	(22)
Southern GBR - Great Keppel Islands																						
22	NKI 009	2.9348	0.0012	3.499	0.005	130.60	0.50	0.05132	0.00018	1.1443	0.0010	5.006	0.019	4.977	0.020	4913	20	1.1464	0.0010	146.4	1.0	MC-ICP-MS/2014[(d)]
23	GKI 001	3.2827	0.0012	2.311	0.003	131.00	0.60	0.03039	0.00015	1.1445	0.0007	2.938	0.015	2.919	0.015	2856	15	1.1457	0.0007	145.7	0.7	MC-ICP-MS/2014[(d)]
24	GKI 005	3.1125	0.0010	7.356	0.011	23.50	0.20	0.01827	0.00011	1.1448	0.0009	1.756	0.011	1.704	0.017	1640	17	1.1456	0.0009	145.6	0.9	MC-ICP-MS/2014[(d)]
25	GKI 003	2.9822	0.0011	4.413	0.006	33.50	0.30	0.01632	0.00012	1.1456	0.0008	1.566	0.012	1.532	0.015	1468	15	1.1463	0.0008	146.3	0.8	MC-ICP-MS/2014[(d)]
26	HUMP 018	2.8587	0.0014	0.434	0.001	219.20	1.90	0.01096	0.00009	1.1468	0.0007	1.048	0.009	1.041	0.009	977	9	1.1473	0.0007	147.3	0.7	MC-ICP-MS/2014[(d)]
27	HUMP 019	3.0813	0.0014	0.411	0.001	246.70	2.00	0.01085	0.00008	1.1460	0.0013	1.039	0.008	1.032	0.008	968	8	1.1464	0.0013	146.4	1.3	MC-ICP-MS/2014[(d)]
SCS - Xisha (or Paracel) Islands																						
28	YXO-1	2.6113	0.0023	0.307	0.001	1559.17	9.22	0.06038	0.00021	1.1504	0.0016	5.856	0.022	5.853	0.022	5798	22	1.1529	0.0016	152.9	1.6	TIMS/2005
29	YXO-5	2.5675	0.0021	0.345	0.002	1307.55	12.29	0.05795	0.00021	1.1490	0.0017	5.622	0.022	5.618	0.022	5563	22	1.1514	0.0017	151.4	1.7	TIMS/2005
30	YXD-2	2.6351	0.0031	2.629	0.010	127.90	1.05	0.04205	0.00023	1.1506	0.0022	4.046	0.024	4.020	0.024	3965	24	1.1523	0.0022	152.3	2.2	TIMS/2005
31	YXO-3	2.8764	0.0053	0.258	0.002	1048.96	19.85	0.03102	0.00039	1.1531	0.0037	2.964	0.039	2.962	0.039	2908	39	1.1544	0.0037	154.4	3.7	TIMS/2004
32	YXD-4	2.8418	0.0026	0.541	0.004	356.07	3.91	0.02234	0.00011	1.1500	0.0014	2.133	0.011	2.128	0.011	2074	11	1.1510	0.0014	151.0	1.4	TIMS/2004
33	YXD-5	2.6957	0.0037	0.713	0.003	246.37	1.39	0.02147	0.00007	1.1516	0.0021	2.045	0.008	2.039	0.008	1985	8	1.1525	0.0021	152.5	2.1	TIMS/2004
34	YXS-4	2.7296	0.0029	1.092	0.004	43.24	0.95	0.00570	0.00011	1.1516	0.0014	0.540	0.010	0.529	0.011	476	11	1.1519	0.0015	151.9	1.5	TIMS/2003
35	YXS-20	2.5007	0.0023	1.592	0.005	16.16	0.20	0.00339	0.00003	1.1508	0.0019	0.321	0.003	0.304	0.005	246	5	1.1509	0.0019	150.9	1.9	TIMS/2008
SCS - Yongshu Reef, Nansha (or Spratly) Islands																						
36	NY1-15-5/6	2.9961	0.0025	0.102	0.0003	7456.35	30.00	0.08340	0.00017	1.1457	0.0013	8.206	0.020	8.205	0.020	8148	20	1.1492	0.0013	149.2	1.3	TIMS/2007
37	NY2-16-7/7	2.9931	0.0021	0.314	0.001	2343.34	16.00	0.08110	0.00027	1.1419	0.0009	8.001	0.029	7.998	0.029	7941	29	1.1451	0.0009	145.1	0.9	TIMS/2007
38	NY2-16-1/7	2.9050	0.0018	0.653	0.002	1003.79	5.30	0.07437	0.00026	1.1468	0.0011	7.281	0.027	7.275	0.027	7218	27	1.1499	0.0011	149.9	1.1	TIMS/2007
39	YSO-02-6	2.8373	0.0020	0.756	0.003	634.63	3.10	0.05573	0.00021	1.1506	0.0018	5.394	0.022	5.387	0.022	5332	22	1.1530	0.0018	153.0	1.8	TIMS/2005
40	YSO-02-7	2.3912	0.0019	0.757	0.011	492.30	7.50	0.05139	0.00035	1.1448	0.0020	4.990	0.036	4.982	0.036	4927	36	1.1469	0.0020	146.9	2.0	TIMS/2005
41	NY4-2-279	3.4056	0.0015	0.498	0.003	552.57	3.30	0.02665	0.00009	1.1486	0.0014	2.551	0.009	2.548	0.010	2494	10	1.1497	0.0014	149.7	1.4	TIMS/2004
	NY4-2-279 rep	3.4167	0.0024	0.283	0.001	969.25	2.70	0.02645	0.00007	1.1477	0.0017	2.534	0.008	2.532	0.008	2478	8	1.1488	0.0017	148.8	1.7	TIMS/2004
	NY4-2-279 mean															2485	8					
42	YSO-02-11	2.8422	0.0017	1.494	0.002	95.15	0.45	0.01648	0.00006	1.1482	0.0010	1.572	0.006	1.558	0.009	1505	9	1.1489	0.0010	148.9	1.0	TIMS/2003
43	Huanglu-1	2.3629	0.0036	1.906	0.021	49.78	0.36	0.01323	0.00021	1.1448	0.0017	1.264	0.020	1.231	0.021	1178	21	1.1453	0.0017	145.3	1.7	TIMS/2003
44	YSO-02-19	2.4155	0.0010	0.292	0.001	212.99	1.20	0.00848	0.00003	1.1495	0.0012	0.805	0.003	0.802	0.004	749	4	1.1499	0.0012	149.9	1.2	TIMS/2003

Note:

[(a)] - ^{230}Th age in kyr relative to year of measurement

[(b)] - ^{230}Th age in yr relative to AD 1950

[(c)] - Date reported in Leonard et al. (2018)

[(d)] - Date reported in Leonards et al. (2016)

Supplementary Table S3 - AMS ^{14}C results showing the ΔR, R and $\Delta^{14}C$ values for coral samples from the SCS and GBR

	Lab ID	Sample ID	Taxon	$\delta^{13}C$ (‰)	^{230}Th Age		Measured		ΔR (^{14}C yr)[a]		R (^{14}C yr)[b]		$\Delta^{14}C$ (‰)[c]	
					mean	2σ	mean	1σ	mean	1σ	mean	1σ	mean	1σ
	(1)	(2)	(3)	(4)	(5)	(6)	(7)	(8)	(11)	(12)	(15)	(16)	(17)	(18)
Northern GBR - Clerke Island														
1	OZU732	CLE S2RFC1	*unidentifiable coral*	-1.0	6268	37	6299	26						
		CLE S2RFC1 rep		-2.0	6301	93	6266	28						
		CLE S2RFC1 mean			6273	35	6284	19	425	46	804	72	-23.2	4.7
2	OZU731	CLE S1C2	*Faviid*	-0.5	187	5	552	19	14	19	334	21	-45.1	2.3
Northern GBR - Gore Island														
3	OZU735	GOR N021	*Porites*	-1.7	7038	48	6611	27	88	44	404	47	28.8	6.9
4	OZU736	GOR S2RFC4	*Acropora*	-2.6	7023	52	6785	32						
		GOR S2RFC4 rep		-2.5	6821	187	6737	30						
		GOR S2RFC4 mean			7009	52	6759	24	255	44	570	54	6.4	7.0
5	OZU734	GOR N019	*Porites*	-1.7	5757	43	5699	24						
		GOR N019 rep		-1.7	5626	44	5745	30						
		GOR N019 mean			5694	65	5718	23	376	64	696	72	-22.8	8.2
6	OZU733	GOR N010	*Porites*	-1.9	5580	44	5162	27	-55	57	300	113	32.9	6.5
7	OZV809	GOR 005	*Porites*	-0.8	4284	47	4083	29	-108	42	171	47	9.9	6.8
8	OZV812	GOR N006	*Porites*	-0.8	4065	42	3938	22	-105	36	186	47	1.5	5.8
9	OZV811	GOR N004	*Porites*	-1.6	3510	37	3540	22	-76	38	208	41	-16.0	5.2
10	OZV810	GOR N002	*Porites*	-1.2	2815	33	3030	26	-30	42	258	46	-36.0	4.9
11	OZV813	GOR S1C4	*Acropora*	-1.2	1428	6	1808	18	-87	18	200	24	-51.0	2.3
12	OZU737	GOR S3C2	*Faviid?*	-1.2	237	21	544	23	-32	36	379	36	-38.3	3.7
Northern GBR - Haggerstone Island														
13	OZU739	HAG 016	*Porites*	-0.9	5096	36	4778	29	-36	34	232	45	21.9	5.8
14	OZU738	HAG 002	*Porites*	-1.1	4592	33	4503	28	69	35	350	44	-5.1	5.3
15	OZV815	HAG 003	*Porites*	-1.9	3999	28	3878	23	-114	30	145	45	1.0	4.5
16	OZV816	HAG 006	*Porites*	-1.1	3874	38	3847	21	-54	39	222	51	-10.2	5.2
17	OZU740	HAG S2RFC1	*Acropora*	-0.3	934	8	1467	24	71	26	391	33	-67.2	2.9
18	OZU741	HAG S3C2	*Porites*	-2.5	643	7	1121	24	50	28	424	30	-59.9	2.9
Northern GBR - Alexandra Reef														
19	OZV804	ALR 043	*Porites*	-2.7	4473	48	4319	28	-26	52	260	58	3.4	6.8
Northern GBR - High Island														
20	OZU742	HIG 005C	*Porites*	-1.6	6761	62	6237	33	-68	62	250	69	42.3	8.9
21	OZU745	HIG MA015E2	*Porites*	-1.6	6592	39	6257	28						
		HIG MA015E2 rep		-1.7	6616	21	6269	30						
		HIG MA015E2 mean			6611	18	6263	20	96	26	438	34	20.2	3.4

	(1)	(2)	(3)	(4)	(5)	(6)	(7)	(8)	(11)	(12)	(15)	(16)	(17)	(18)
Southern GBR - Great Keppel Islands														
22	OZV819	NK1 009	*Porites*	-2.1	4913	20	4652	24	-50	26	231	35	15.3	3.9
23	OZV805	GK1 001	*Porites*	-0.3	2856	15	3085	25	-8	28	282	43	-37.8	3.4
24	OZV807	GK1 005	*Porites*	-1.2	1640	17	2015	21	-54	24	228	27	-51.2	3.1
25	OZV806	GK1 003	*Porites*	-0.9	1468	15	1836	27	-76	28	217	30	-49.7	3.7
26	OZV817	HUMP 018	*Cyphastrea*	1.5	977	9	1366	18	-80	20	215	25	-50.6	2.4
27	OZV818	HUMP 019	*Cyphastrea*	2.3	968	8	1402	18	-35	20	264	28	-55.8	2.3
SCS - Xisha (or Paracel) Islands														
28	OZM065	YXO-1	*Porites*	-1.3	5798	22	5593	35	173	37	520	39	5.2	5.1
29	OZM064	YXO-5	*Porites*	-0.7	5563	22	5283	35	88	48	535	51	15.4	5.2
30	OZM060	YXD-2	*Porites*	-0.6	3965	24	4009	41	34	44	364	51	-19.2	5.8
31	OZM059	YXO-3	*Porites*	-1.1	2908	39	3216	33	82	46	404	47	-47.4	5.9
32	OZM057	YXD-4	*Porites*	-1.5	2074	11	2622	36	192	36	519	38	-72.7	4.3
33	OZM056	YXD-5	*Porites*	-1.2	1985	8	2440	36	73	37	418	39	-61.7	4.3
34	OZM051	YXS-4	*Porites*	-0.3	476	11	787	34	-52	39	410	38	-39.5	4.2
35	OZM050	YXS-20	*Porites*	-1.1	246	5	523	30	-48	31	420	31	-34.6	3.7
SCS - Yongshu Reef, Nansha (or Pratly) Islands														
36	OZM068	NY1-15-5/6	*Porites*	-0.7	8148	20	7974	42	290	48	679	51	-7.0	5.7
37	OZM067	NY2-16-7/7	*Porites*	-1.5	7941	29	7848	40	368	54	756	71	-16.3	5.9
38	OZM066	NY2-16-1/7	*Porites*	0.2	7218	27	7081	40	391	50	807	48	-8.3	5.9
39	OZM063	YSO-02-6	*Porites*	0.7	5332	22	4898	33	-100	40	216	63	35.9	5.1
40	OZM062	YSO-02-7	*Porites*	0.0	4927	36	4760	37	48	46	380	44	3.4	6.3
41	OZM058	NY4-2-279	*Acropora*	-1.5	2494	10	2834	33						
		NY4-2-279 rep			2478	8								
		NY4-2-279 mean			2485	8	2834	33	62	34	386	37	-50.9	4.1
42	OZM054	YSO-02-11	*Porites*	0.0	1505	9	1835	33	-106	34	268	36	-45.3	4.1
43	OZM053	Huanglu-1	*Porites*	-1.0	1178	21	1619	35	15	40	389	55	-57.3	4.7
44	OZM052	YSO-02-19	*Porites*	-2.1	749	4	1271	32	53	32	414	33	-65.4	3.8

Note:

[(a)] - ΔR and associated uncertainty calculated using the online *deltar* software (Reimer and Reimer, 2017) and the Marine13 data (Reimer et al., 2013)

[(b)] - R and associated uncertainty calculated using the software *ResAge* (Soulet 2015) and IntCal13 (Reimer et al., 2013) and SHCal13 (Hogg et al., 2013) for the SCS and GBR, respectively

[(c)] - Age-corrected $\Delta^{14}C$ was calculated using equation (3) in Hua et al. (2015). Both age uncertaities (^{230}Th and ^{14}C) were taken into account when calculating 1σ uncertainty for $\Delta^{14}C$

References

Hogg, A.G., Hua, Q., Blackwell, P.G., Niu, M., Buck, C.E., Guilderson, T.P., Heaton, T.J., Palmer, J.G., Reimer, P.J., Reimer, R.W., Turney, C.S.M., Zimmerman, S.R.H., 2013. SHCal13 Southern Hemisphere calibration, 0-50,000 cal yr BP. Radiocarbon 55, 1889-1903, doi:10.2458/azu_js_rc.55.16783.

Hua, Q., Webb, G.E., Zhao, J.-x., Nothdurft, L.D., Lybolt, M., Price, G.J., Opdyke, B.N., 2015. Large variations in the Holocene marine radiocarbon reservoir effect reflect ocean circulation and climatic changes. Earth Planet. Sci. Lett. 422, 33-44, doi:10.1016/j.epsl.2015.03.049.

Leonard, N.D., Zhao, J.-x., Welsh, K.J., Feng, Y.-x., Smithers, S.G., Pandolfi, J.M., Clark, T.R., 2016. Holocene sea level instability in the southern Great Barrier Reef, Australia: high-precision U-Th dating of fossil microatolls. Coral Reefs 35, 625-639, doi:10.1007/s00338-015-1384-x.

Leonard, N.D., Welsh, K.J., Clark, T.R., Feng, Y.x., Pandolfi, J.M., Zhao, J.x., 2018. New evidence for "far-field" Holocene sea level oscillations and links to global climate records. Earth Planet. Sci. Lett. 487, 67-73, doi:10.1016/j.epsl.2018.02.008.

Reimer, R.W., Reimer, P.J., 2017. An online application for ΔR calculation. Radiocarbon 59, 1623-1627, doi:10.1017/RDC.2016.117.

Reimer, P.J., Bard, E., Bayliss, A., Beck, J.W., Blackwell, P.G., Bronk Ramsey, C., Buck, C., Cheng, H., Edwards, R.L., Friedrich, M., Grootes, P.M., Guilderson, T.P., Haflidason, H., Hajdas, I., Hatteé, C., Heaton, T.J., Hoffmann, D.L., Hogg, A.G., Hughen, K.A., Kaiser, K.F., Kromer, B., Manning, S.W., Niu, M., Reimer, R.W., Richards, D.A., Scott, E.M., Southon, J.R., Staff, R.A., Turney, C.S.M., van der Plicht, J., 2013. IntCal13 and Marine13 radiocarbon age calibration curves 0-50,000 years cal BP. Radiocarbon 55, 1869-1887, doi:10.2458/azu_js_rc.55.16947.

Soulet, G., 2015. Methods and codes for reservoir-atmosphere ^{14}C age offset calculations. Quat. Geochronol. 29, 97-103, doi:10.1016/j.quageo.2015.05.023.